



Critical interface between inorganic solid-state electrolyte and sodium metal

Bin Tang¹, Prem Wicram Jaschin², Xin Li³, Shou-Hang Bo^{2,*}, Zhen Zhou^{1,4,*}

¹ School of Materials Science and Engineering, Institute of New Energy Material Chemistry, Key Laboratory of Advanced Energy Materials Chemistry (Ministry of Education), Renewable Energy Conversion and Storage Center (ReCast), Nankai University, Tianjin 300350, PR China

² University of Michigan – Shanghai Jiao Tong University Joint Institute, Shanghai Jiao Tong University, 800 Dong Chuan Rd., Minhang District, Shanghai 200240, PR China

³ John A. Paulson School of Engineering and Applied Sciences, Harvard University, Cambridge, MA 02138, USA

⁴ Engineering Research Center of Advanced Functional Material Manufacturing of Ministry of Education, School of Chemical Engineering, Zhengzhou University, Zhengzhou 450001, China

With widening applications in next-generation energy storage systems, rechargeable secondary batteries with enhanced safety and energy density are imperative for technological advancements. All-solid-state sodium batteries can be a promising low-cost and high-energy-density candidate, provided that stable cycling of the energy-dense Na metal anode can be achieved. However, the interface between Na metal and solid-state electrolyte remains a challenging problem. Here we comprehensively review various physical and chemical properties of different types of sodium-based solid-state electrolytes including sodium β -alumina, Na super ionic conductors (NASICON), chalcogenides, perovskites, complex hydrides and antiperovskites, and discuss some critical common factors that affect the Na/electrolyte interface stability. We also summarize the state-of-art strategies to engineer the interface for better electrochemical performances.

Keywords: Inorganic solid-state electrolyte; Interface stability; Sodium metal; Solid electrolyte interphase; Mixed ionic electronic conducting interphase.

Introduction

All aspects of our modern society now substantially rely on the improvement of energy production and storage technologies. Research and development on reliable, safe and economical energy storage technologies have been extensively performed, which often have to balance with the ever-growing, equally important need for high energy and power densities [1]. Among the various existing battery systems, one of the most popular ones is the liquid-electrolyte-based batteries, but they are flammable and hazardous. Tremendous efforts have been focused on developing all-solid-state batteries to improve safety and to obtain high-energy-density systems [2–8]. An all-solid-state battery houses a thin film of ceramic, polymer or polymer–ceramic

composite as solid-state electrolyte, which exhibits high ionic conductivity, sandwiched between two solid electrodes of mixed active and electrolyte materials [9–11].

In the present commercial landscape, lithium ion batteries have been the dominant battery technology and remain ubiquitous in our everyday life. However, sustainability issue causes an increasing concern owing to the surging demands and limited global lithium reserves [12]. In this context, sodium-based batteries prove themselves to be one of the most viable alternatives, as sodium possesses similar chemical and physical properties to lithium and is abundant in nature [13]. Similar in design to a Li-ion battery, a typical sodium-ion battery [14–16] comprises a cathode [17,18] which is made of metal oxides [19–35], sulfates/sulfides [36–40] or phosphates [41–49]; an anode [50,51] in the form of hard carbon [52–60] or metals/alloys [61–65]; and, a sodium ion conducting electrolyte [66,67]. Recent reports on

* Corresponding authors.

E-mail addresses: Bo, S.-H. (shouhang.bo@sjtu.edu.cn), Zhou, Z. (zhouzhen@nankai.edu.cn).

the fabrication of sodium-ion batteries based on non-aqueous electrolytes have shown much promise [68]. Furthermore, Faradion Limited has successfully made a first-generation sodium-ion battery of 400 Wh energy and demonstrated its application in an E-bike [69]. Recently, a group of scientists in China have further demonstrated the use of sodium-ion batteries in low-speed electric vehicles [70].

The demand for high energy density calls for an approach towards the use of all-solid-state sodium metal batteries [71–74]. Na metal anode possesses high theoretical capacity (1165.8 mAh g⁻¹, as compared with 270.5 mAh g⁻¹ for hard carbon (Na₄C₃₃) [75]) and low electrochemical potential (–2.7 V vs standard hydrogen electrode). By changing the hard carbon anode into Na metal, a full cell based on Na₃V₂(PO₄)₃ cathode (117.6 mAh g⁻¹, 20% porosity filled with liquid electrolyte of approximately 1 g mL⁻¹) and Na metal anode (20% excess) can achieve a cell level energy density of 220 Wh kg⁻¹, which is a 29% increase over that based on hard carbon. However, Na metal suffers from issues of inhomogeneous deposition/stripping and dendrite penetration, similar to those of lithium metal anodes [76–78]. Ceramic solid-state electrolytes with high mechanical strength were proposed to suppress the formation of metal protrusions. Unfortunately, there are only limited reports on fabricating all-solid-state sodium metal batteries for practical applications. The challenges are primarily twofold: one is to acquire high performance solid-state electrolytes (SSEs) with appropriate mechanical strength as well as high ionic conductivity [79–81]; and the other is to construct a stable interface between the solid-state electrolytes and sodium metal [82–84]. We note that the interface stability between cathodes and electrolytes is also difficult to achieve [85–88], which is, however, beyond the scope of this review.

Despite the discovery of several compounds that exhibit high sodium ion conductivity, compatibility issues between the sodium metal anode and solid-state electrolyte has been the major drawback, as it significantly affects the stability and coulombic efficiency of charge–discharge cycles [89–91]. Thus, it is imperative to understand the chemical, mechanical and electrochemical properties of the solid-state electrolyte, which are often coupled together, and its interface with sodium metal [92–97]. A stable Na/electrolyte interface should resist the deformation caused by the substantial volume variation of Na metal during the charging/discharging process, and should always remain in close contact with Na metal and solid-state electrolytes. Such volume variation at a reasonable area capacity of 1 mAh cm⁻² corresponds to 8.8 μm thickness of Na metal plating/stripping if assuming a fully dense and smooth deposition.

Moreover, in a liquid-electrolyte based cell, sodium dendrite deposition at the electrode during cycling has been observed to adopt different morphologies – sometimes needle-like structures [98,99] that grow up to a few microns in length and sometimes a mossy-like appearance [99,100]. Although, the underlying mechanism of these varied growth patterns is yet to be fully understood, the roots of these dendrites are sources for “dead sodium” that could deteriorate the coulombic efficiency over a period of time [101]. The electrochemo-mechanical strength of solid-state electrolytes becomes imperative to suppress dendritic growth as loss of contact is much more feasible here. Over several

hundreds of charging–discharging cycles, the electrolyte must endure a repetitive volume change occurring at the electrodes. This dynamical strain variation at the electrolyte–anode interface could lead to detrimental deformation of the electrolyte. Therefore, mechanical stability of the solid-state electrolyte plays a critical role in attaining reliable performances from the solid-state batteries.

Meanwhile, a stable Na/electrolyte interface should be passivating, *i.e.*, electronically insulating, which prevents the continuous rise of cell impedance caused majorly by the reaction between Na metal and solid-state electrolyte. An ideal interface here is hence similar to what was discussed in conventional lithium-ion batteries, which permits the lithium ion diffusion but not the electron. In cases where Na metal is thermodynamically stable against the solid-state electrolytes, the interfacial wettability of Na metal and solid-state electrolyte should be considered [101–103].

In this review, we introduce different types of sodium solid-state electrolytes through a perspective of their interface stability against sodium metal. We discuss the thermodynamic properties of solid-state electrolytes and their impact on the interface stability against Na metal. Furthermore, the inorganic solid-state electrolytes are rated based on their mechanical and chemical properties against sodium metal, suggesting strengths and weaknesses of each class of solid-state electrolyte. In the end, methods of alleviating and minimizing the unstable interfacial effects are discussed.

Interface stability

When a solid-state electrolyte comes in contact with sodium metal, there are three main issues that can occur at the interface during the electrochemical cycling – formation of compositionally different phases, *i.e.*, the interphases; insufficient contact between electrode and electrolyte; and finally, metal dendrite formation and penetration through the electrolyte. In the first scenario, owing to the highly reducing metal, formation of a thin layer of interphases between the electrode and the electrolyte is often observed, which controls the performance of the electrochemical cell. Such interphases are generated as a consequence of electrolyte decomposition. Wenzel et al. categorized interfaces in solid-state batteries into three types with respect to their stability [104–108].

Type I – A thermodynamically stable interface with no electrochemical/chemical reactions.

Type II – A non-passivating interface with electronic and ionic conductivity bespoken as mixed ionic electronic conducting interphase (MCI).

Type III – A steady solid (or cathode) electrolyte interphase (SEI (or CED)) with high ionic conductivity but insignificant electronic conductivity.

To ensure long-term stable battery operation, interfaces of type I or type III are needed.

In the second scenario where there is insufficient contact, a high interfacial resistance that negatively impacts the cycling performance of the cell is frequently observed. Furthermore, undesirable dendrite formation could also occur. One way to circumvent this is to melt the metal on the solid-state electrolyte. The melting point of Na metal is 371 K, which is much lower

than that of Li metal (454 K). Nevertheless, several factors could affect this method, such as wettability at the electrolyte surface and chemical stability of the electrolyte against the metal at elevated temperatures. Insufficient contact can also arise from the substantial volume change because of repeated Na metal deposition/stripping, placing even more stress on the robustness of the Na/electrolyte interface.

Lastly, the mechanical strength of the solid-state electrolyte is an important characteristic that could be strongly correlated with the dendrite growth across the electrolyte during repetitive cycles [109]. Continuous dendrite growth can eventually lead to short-circuiting of the cell. The following sections present a brief introduction to the chemical and mechanical properties of the interface.

(Electro)chemical stability

Chemical instability of the solid-state electrolyte arises from its reduction by the metallic sodium anode. In particular, when the SSE contains easily reductive metal element(s), the reduction process often leads to the generation of metals or alloys at the metal/electrolyte interface. This eventually results in the formation of a detrimental MCI that continuously consumes the electrolyte and the metal.

Computationally, the interface stability between Na metal and the solid-state electrolyte as well as the associated reaction products can be evaluated through Na grand potential phase diagram [110–113]. Today, such a methodology has been implemented in materials databases such as Materials Project [114], which is accessible for free to the scientific community. The thermodynamic grand potential phase diagram approach does not consider reaction kinetics and relies on the accurate determination of energies for all relevant phases in the selected phase diagram. Mechano-electrochemical interaction has recently been integrated into a generalized computational approach by Li and co-workers [115,116] to further predict the change of such standard thermodynamic interface stability in response to different materials levels of mechanical constrictions, which is a general method that can be applied to both Li and Na based solid-state electrolytes and interfaces. Molecular dynamics (MD) simulation is an alternative approach to evaluate the metal/electrolyte interface stability. However, it heavily depends on the initial input of materials structure and can be trapped at local minimum during simulations.

On the experimental side, Janek [105], Meng [117], Ceder [118] and Goodenough [119] groups have realized *in-situ* observation of the interface product, which is also remarkable research progress for solid-state batteries. A variety of techniques have been utilized in the solid-state batteries, including electrochemical impedance spectroscopy (EIS), X-ray photoelectron spectroscopy (XPS), time-of-flight secondary ion mass spectrometer (TOF-SIMS), *in-situ* scanning transmission electron microscopy (STEM) and electron energy loss spectroscopy (EELS), synchrotron X-ray depth profiling and solid-state nuclear magnetic resonance (ss-NMR) [120] for observing various characteristics of the interface [83,121].

Mechanical stability

The Young's modulus of a solid-state electrolyte is considered to be of key importance. The shear modulus of the electrolyte is also

responsible for dendrite formation on the anode surface during cycling. In order to suppress dendrite formation, Monroe and Newman [122] as well as Albertus et al. [123] suggested that the shear modulus should be at least twice that of metal [124]. The shear modulus of bulk Na metal is 3.3 GPa, which is much lower than that of bulk lithium metal (4.2 GPa). However, Xu et al. [125] discovered that Li has significant anisotropy in mechanical properties. Along different orientations, the elastic modulus (3.00–21.2 GPa) and shear modulus (1.46–8.78 GPa) vary in a broad range. This leads to different propensities for dendrite formation and growth. In reality, the dendrite deposition could still occur even if the solid-state electrolyte satisfies Monroe's criterion, because there are other factors that can also induce dendrite formation. For example, porosity at the electrolyte/anode interface [126–128] and high electronic conductivity at the grain boundaries or the interface affect the formation of dendrites [129–131]. Meanwhile, complexity in microstructures may change the local modulus distribution of materials, which may loosen Monroe's criterion in such cases. Generally speaking, Monroe's criterion might be viewed as a helpful guideline, but not a strict condition for selecting a viable solid-state electrolyte.

Hardness (H) is another important trait that needs to be addressed in a solid-state electrolyte. Several models have been proposed to estimate the hardness of a material. Hardness of the interface indicates its ability to tolerate the volume expansion of anodes and cathodes. Hardness thus affects the surface contact between solid-state electrolytes and sodium. Meanwhile, hardness is negatively correlated with fracture toughness K_{Ic} . K_{Ic} reflects the susceptibility to fracture and hence passage of Li dendrites, as demonstrated in the equation:

$$K_{Ic} = k \left(\frac{E}{H} \right)^{1/2} \frac{P}{c^{3/2}}$$

where k is a constant, E is elastic modulus, P is the applied load, and c is the track length [132]. Hardness represents the resistance to elastic and plastic deformation, or failure under external force.

Mechanical properties of a solid-state electrolyte vary between the grain and grain boundaries of a material resulting in heterogeneity, which is suggested to be one origin of mechanical failure at the metal/electrolyte interface [104,133]. A typical polycrystalline inorganic solid-state electrolyte comprises a collection of grains glued together across grain boundaries [134]. There seems to be an inherent heterogeneity in terms of the properties between the bulk grains and the grain boundaries, especially in their sodium ion concentration, ionic conduction and mechanical strength. The implication is that grain boundaries can be vulnerable to various mechanical failures and being at a higher state of stress makes fracture propagation easier [135]. One of the major concerns in this regard is, thus, the fracture of the solid-state electrolyte itself [136]. The concentrated stress on the grain boundaries can also be seen as favorable sites for dendritic deposition and growth across the electrolyte [125,137]. Grain boundaries are particularly vulnerable to dendritic growth owing to a reduced shear modulus (around 0.2–0.6 times the bulk value) and relatively larger local current densities around the region [138,139].

Although the mechanical strength of the material is important in realizing suppression of dendritic growth and to nullify

crack propagation in a solid-state electrolyte, the metallic deposition at the electrode–electrolyte interface during multiple electrochemical cycles can adversely affect the mechanical stability of the material [140]. Such “chemo-mechanical” effects are influenced by the inhomogeneous metallic deposition at the anode or electrolyte decomposition at the interface that could lead to non-uniform potential distribution [141]. This phenomenon has been observed to induce void formation that drives the dendrite formation at the interface in several Li-based systems [93,142–144]. The occurrence of such voids during lithium plating/stripping can be understood from the perspective of critical stripping current densities of the material [104,145]. The dynamics of the charge transfer between the metallic anode and the solid-state electrolyte is dominated by the vacancy diffusion process for $\text{Li}_6\text{PS}_5\text{Cl}$ and sodium β'' -alumina systems. If the stripping of the metal or the dissolution of the metal occurs at a local current density that does not exceed its vacancy diffusion limit, one can expect a continuous and homogenous flow of atoms across a stable interface. However, at an applied local current density larger than the vacancy diffusion limit, pore formation is induced by the supersaturation and accumulation of vacancies. The contact loss caused by these pores could be remedied by an external applied pressure accounting for the plastic deformation of lithium metal by annihilating the created pores. Reports suggest that a stack pressure of 5–7 MPa could be preferable for smooth electrochemical cycling for Li metal stripping and plating [145,146].

Higher stack pressure on the reported Li metal–solid-state electrolyte ($\text{Li}_6\text{PS}_5\text{Cl}$) system is short-circuited more easily. On the other hand, a stack pressure of 100 MPa was found to be highly effective, and devoid of any dendrite formation or defects, for plating and stripping of lithium across a $\text{Li}_{10}\text{GeP}_2\text{S}_{12}$ (LGPS) system as the electrolyte and the lithium–graphite composite was used as the anode. This composite anode–LGPS electrolyte set-up displayed high current densities, of the order of 10 mA cm^{-2} , during electrochemical cycling. Such improved stability was achieved due to an enhanced interfacial chemical stability with the presence of graphite, and an enhanced interfacial electrochemical stability from stronger mechanical constriction effect induced by the high stack pressure, in addition to the conventional understanding of improved interfacial contact [147]. Hence, it is imperative to understand such mechano-chemical effects over the sodium solid–electrolyte counterparts. In addition, the electrolyte needs to withstand the stress induced by the volume changes that occur at the electrodes. These volume changes could contribute to contact loss at the electrode–electrolyte interface resulting in high interfacial resistance and, eventually, capacity fade and poor cyclability [148].

Interestingly, in a recent effort by Jolly et al. [149], a linear dependency between the critical current density and critical pressure required to suppress voids was established for a three-electrode cell based on sodium metal (as the working, counter and reference electrodes) and sodium β'' -alumina as the solid electrolyte. It was observed that for the current density of 2.5 mA cm^{-2} , a critical pressure of above 9 MPa was required for the cell to cycle without loss of contact and void formation. Sodium creep was found to be a necessary and dominant mechanism in these systems for sodium ion transport to occur across

the electrode–electrolyte interface. Consequently, an increase in the rate of creep is required for better electrochemical cyclability by operating at high temperatures or using a more favorable anode design (*i.e.*, sodium alloying). Heinz et al. [150] realized that in a planar cell design of Na– NiCl_2 full cells with a β'' -alumina solid-state electrolyte, reducing pressure during cell closure to less than the fracture strength of the solid-state electrolyte is an effective strategy for restricting adverse chemo-mechanical effects on the battery. As such, several different mechanisms for lithium dendrite formation and electrolyte crack propagation have been investigated from different perspectives, be it defect induced or even dendrite formation in a graphite anode-based full cell solid-state electrolyte system [151,152]. Nevertheless, the understanding of the sodium dendritic formation and propagation across inorganic solid-state electrolytes is still at its budding stages.

Inorganic solid-state electrolytes and their interfacial properties

Inorganic solid-state electrolytes, owing to their high mechanical strength, are a viable option for alkali metal anodes. However, many factors hamper their application in the all-solid-state sodium ion batteries, which include poor interface contact (inducing sluggish kinetic ion transfer within the metal/electrolyte interface), undesirable chemical/electrochemical reactions with alkali metal, modest thermodynamic and mechanical stability of certain solid-state electrolytes. Different solid-state electrolytes face diverse interface issues and challenges that need to be addressed. So, in this section, we present critical interface issues between the inorganic solid-state electrolyte and the sodium metal. The electrolytes have been categorized according to the respective anionic composition.

Sodium β -alumina

The sodium β -alumina solid-state electrolyte was first discovered in 1960s [153]. It possesses an ionic conductivity as high as $1.4 \times 10^{-2} \text{ S cm}^{-1}$ at room temperature (RT) and good thermal properties [154,155]. The β -alumina crystallizes in two types of structure, namely, hexagonal β -alumina [153] and rhombohedral β'' -alumina [156] and the ionic migration in these materials are 2-D in nature. Chemical composition of sodium β -alumina is Na_2O (8–11%)– Al_2O_3 while sodium β'' -alumina is Na_2O (5–7%)– Al_2O_3 . Sodium β'' -alumina consists of spinel blocks made of AlO_4 tetrahedra and AlO_6 octahedra, stacked up along the *c*-axis that form the conduction planes for sodium ion transport. At high temperatures of around 250–350 °C, β -alumina could exhibit an ionic conductivity as high as 1 S cm^{-1} , based on which the high temperature Na–S and ZEBRA (sodium–metal chloride) batteries could be applied in large scale energy storage systems [157,158]. Synthesizing pure β'' -alumina is affected by its thermodynamic instability at high temperatures of processing conditions, resulting in a mixture of β -alumina and Al_2O_3 . Hence, trace amounts of stabilizers (MgO , TiO_2 , Y_2O_3 , or ZrO_2) are used to counter the instability [71,157]. Apart from aluminum oxide, calcium and silicon are prominent impurities found in β'' -alumina in the form of calcium aluminate and sodium aluminum silicate. These secondary phases could adversely affect the ionic conduc-

tivity and wettability of molten sodium anodes and consequently, result in larger interfacial resistance.

To account for the poor contact between the sodium β -alumina and sodium, the battery was operated at a high temperature to melt the sodium and improve the ionic conductivity of β -alumina. Wenzel and co-workers [105] introduced interfacial reactivity benchmarking by the use of time-resolved electrochemical measurements (Fig. 1a) and *in-situ* XPS (Fig. 1b). Time-resolved electrochemical measurements are simple and powerful methods to evaluate the stability of SSEs, as long as a small voltage of about 20 mV is applied to determine the charge transfer resistance. Meanwhile, cyclic voltammetry (CV) was used to observe the changes in the polarization resistance by employing a three-electrode system. The sodium β -alumina demonstrates extremely firm chemical stability against sodium metal and shows no change in the polarization resistance or charge transfer resistance as observed from time resolved impedance spectroscopy and CV measurements. Also, the chemical states of Al and O were maintained during the *in-situ* test for sodium deposition. All these suggest that sodium β -alumina is thermodynamically stable with Na metal, consistent with recent theoretical modeling results [159].

NASICON

The sodium super ionic conductor (NASICON) type solid-state electrolyte was first proposed by Goodenough et al. in 1976 [160]. The structure of $\text{NaZr}_2\text{P}_3\text{O}_{12}$ with the parent composition is such that partial replacement of P by Si has tremendous potential of accommodating more Na ions in the unit cell and thereby, improving the ionic conductivity of the material. NASICON crystallizes in rhombohedral and monoclinic structures with channels large enough to allow 3-dimensional ionic migration. The NASICON system with a composition of $\text{Na}_3\text{Zr}_2\text{Si}_2\text{PO}_{12}$ crystallizes in a monoclinic structure and exhibits a high ionic conductivity of 0.67 mS cm^{-1} at room temperature [161,162]. As more Na^+ ions are incorporated into the structure, the ionic conduction occurs through tetrahedral channels in a concerted manner which helps improve the net ionic conductivity of the material [163]. The optimal amount of inclusion of Na^+ ions in the crystal structure to exhibit enhanced ionic conduction was found to be 3.3 moles of Na per formula unit [164].

The partial or complete substitution of Zr^{4+} sites by aliovalent and isovalent cations (such as Mg^{2+} , Co^{2+} , Al^{3+} , Sc^{3+} , La^{3+} , Ti^{4+} , Hf^{4+} , Nb^{5+} , Ta^{5+} , and V^{5+}) results in varied effects on the transport channel bottlenecks, bulk ionic conduction and grain

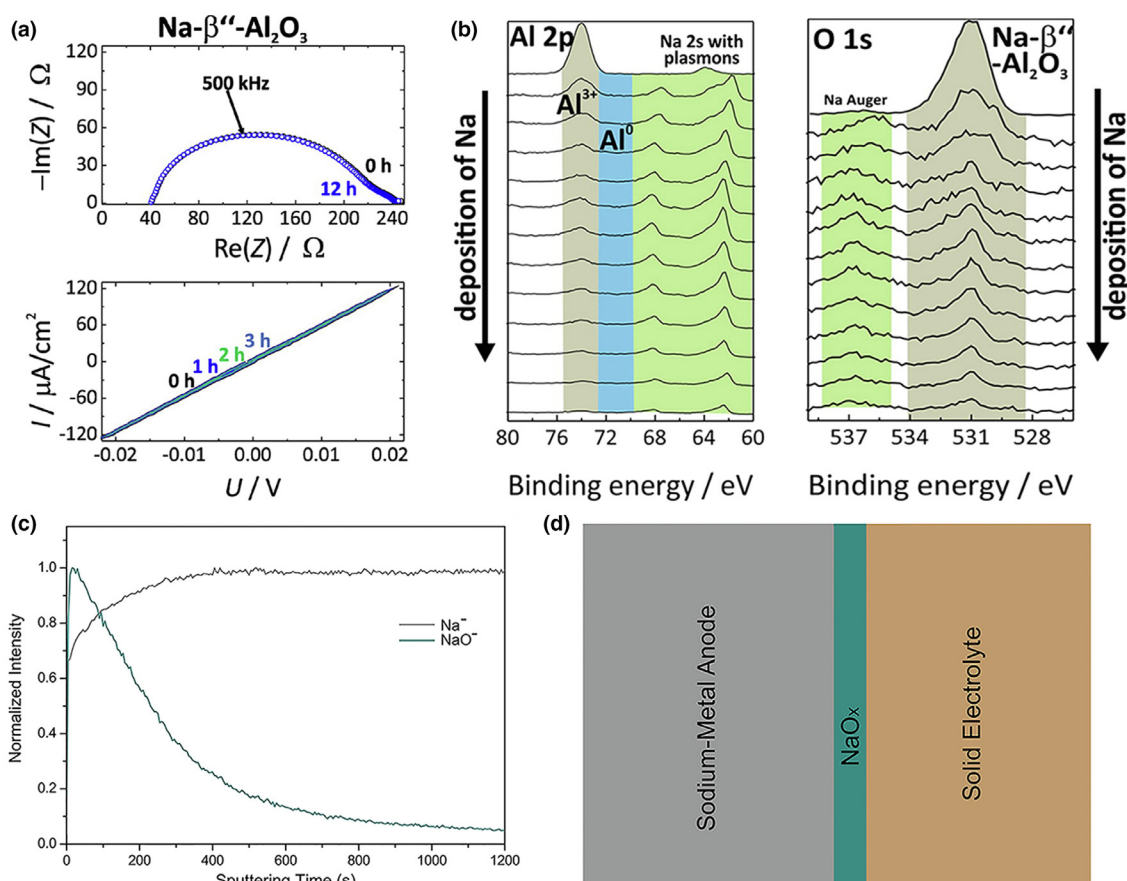


FIGURE 1

(a) EIS and CV data of sodium and sodium- β -alumina with different times of contact. EIS measurements were taken in the frequency range of 7 MHz to 100 MHz and an excitation amplitude of 20 mV. The scan rate of CV tests was set to 1 mV s^{-1} . (b) *In-situ* XPS measurements for sodium deposition on sodium- β -alumina. Reproduced from Ref. [105] with permission, Copyright 2016, American Chemical Society. (c) TOF-SIMS depth profiles of the Na/NASICON interface. (d) Schematic illustrations of the interface of NASICON and sodium. Reproduced from Ref. [119] with permission, Copyright 2018, Elsevier.

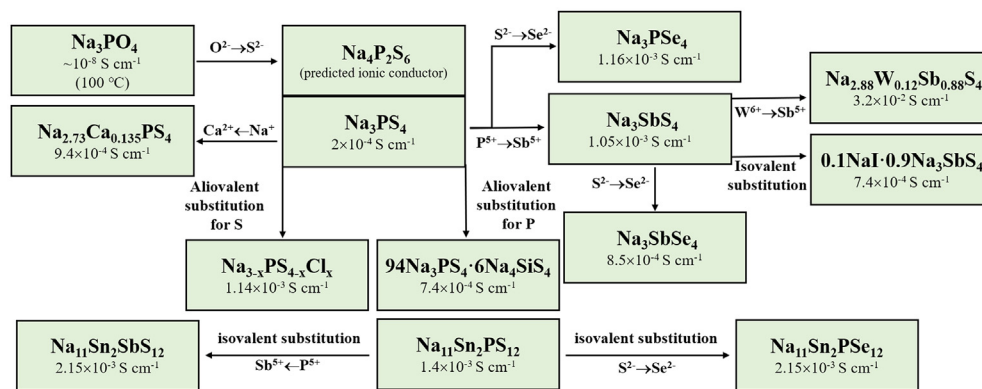


FIGURE 2

Schematic diagram of design strategies for chalcogenide Na^+ superionic conductors and their respective ionic conductivities. This figure is adapted from Reference [171].

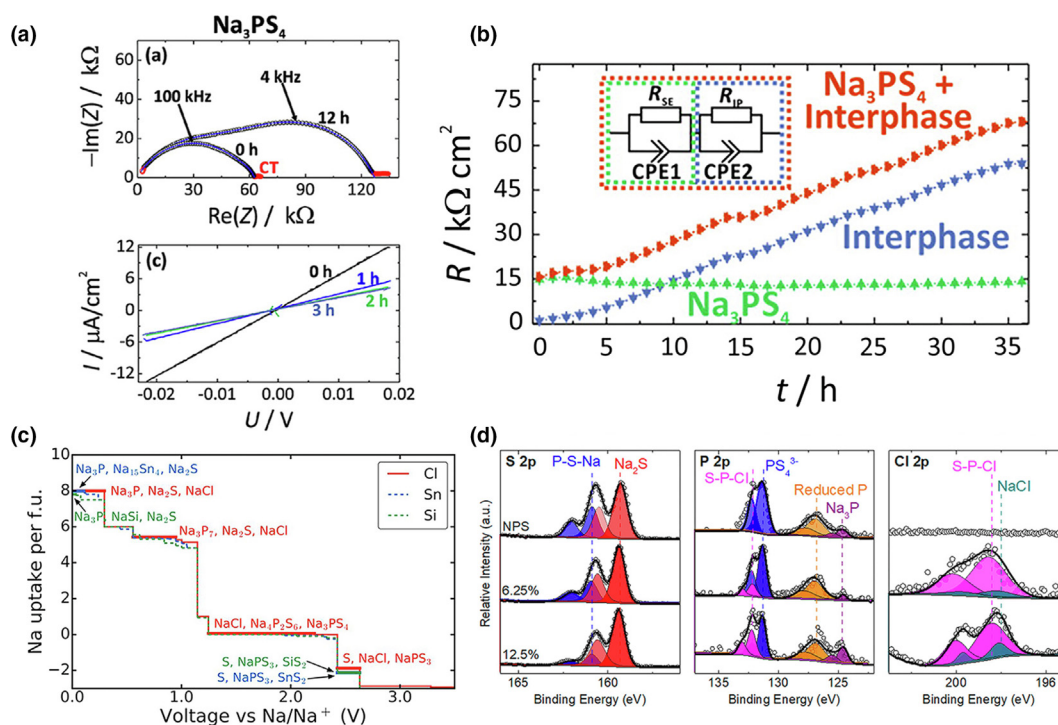


FIGURE 3

(a) EIS and small range CV of $\text{Na}/\text{Na}_3\text{PS}_4/\text{Na}$ symmetric cells for different times. EIS measurements were taken in the frequency range of 7 MHz to 100 MHz and an excitation amplitude of 20 mV. The scan rate of CV tests was set to 1 mV s^{-1} . (b) Time-dependent resistance of Na_3PS_4 and interphase with equivalent circuit models in the inset. Reproduced from Ref. [105] with permission, Copyright 2016, American Chemical Society. (c) Predicted electrochemical decomposition products of Cl-, Sn-, or Si-doped Na_3PS_4 compounds. Reproduced from Ref. [175] with permission, Copyright 2016, Springer Nature. (d) XPS data of S2p, P2p, and Cl2p of pristine Na_3PS_4 and Cl-doped Na_3PS_4 before and after cycling. Reproduced from Ref. [176] with permission, Copyright 2018, American Chemical Society.

microstructures. A comprehensive list of dopants and substitutions in NASICON systems has been covered in other review articles [164,165]. Based on the survey of dopants in the NASICON structure, Guin et al. realized that for the system to yield high ionic conduction, the ionic radii of the substitution elements need to be around 0.72 \AA . This was prominently observed in the Sc^{3+} -doped NASICON which yielded a high ionic conductivity of the order 4 mS cm^{-1} , as the ionic radius compatibility could be attained from Sc^{3+} ion ($r_{\text{ion}} = 0.75 \text{ \AA}$) [166]. On the other hand, the addition of a larger ion La^{3+} has also led to an

enhanced ionic conductivity in the range of 3.4 mS cm^{-1} [167]. Interestingly, the La^{3+} ion was found to be present as a secondary glassy phase along the grain boundaries in the form of $\text{Na}_3\text{La}(\text{PO}_4)_2$ instead of occupying any sites in the parent crystal structure.

Gao et al. [119] used TOF-SIMS to probe the interface between the sodium metal and the NASICON solid-state electrolyte (Fig. 1c, d). TOF-SIMS is a very sensitive surface analytical technique that is well established for detecting the components of a substrate for many industrial and research applications. The

intensity of NaO_x drops off with time which proves that NaO_x exists only on the contact interface between sodium and NASICON. Limited reactions between sodium and NASICON could be attributed to the formation of an ionically passivating film (NaO_x) with a remarkably reduced surface thickness. During the charge–discharge cycles, the passivation film could amend the wettability of the sodium anode on the surface of the solid-state electrolyte, which promotes the dendrite-free deposition of sodium metal. Such wettability is different from the conventional definition (solid–solid direct contact) and should be considered a chemical-reaction-induced wettability, rather than a purely physical process. Similar wettability has been shown to improve ion transport across metal/electrolyte interfaces in a wide range of systems [168–170].

Chalcogenides

Chalcogenide SSEs with high ionic conductivity have appeared to be suitable replacement for liquid electrolytes. Their suppleness allows them to easily obtain close-grained pellets via cold pressing. This particular trait offers them superiority over other electrolyte systems, as versatile geometries in full cell assembly could be achieved. Chalcogenide SSEs are designed based on the strength of Na_3PO_4 . Using aliovalent or isovalent substitution of P and/or O by elements with larger atomic radii, composition and ionic conductivities of these materials can be systematically tuned. Sodium chalcogenide conductors derived from the parent composition include Na_3PS_4 , $\text{Na}_{3-x}\text{PS}_{4-x}\text{Cl}_x$, $\text{Na}_4\text{P}_2\text{S}_6$, $\text{Na}_3\text{PS}_x\text{Se}_{4-x}$, Na_3SbS_4 , $\text{Na}_{11}\text{Sn}_2\text{PS}_{12}$, Na_3PSe_4 , Na_3SbSe_4 , $\text{Na}_{11}\text{Sn}_2\text{SbS}_{12}$, $\text{Na}_{11}\text{Sn}_2\text{PSe}_{12}$ and the glass–ceramic $94\text{Na}_3\text{PS}_4 \cdot 6\text{Na}_4\text{SiS}_4$ (Fig. 2).

Na_3PS_4 was the first reported sulfide superionic electrolyte. Na_3PS_4 reveals two crystal structures: tetragonal phase ($P-42_1c$; $a = b = 6.9520 \text{ \AA}$, $c = 7.0757 \text{ \AA}$) and cubic phase ($I-43m$; $a = b = c = 7.0699 \text{ \AA}$). For the cubic phase, Na partially occupies 6b site and 12d site. The tetragonal phase synthesized at low temperature (*i.e.*, $251 \text{ }^\circ\text{C}$) exhibited a moderate ionic conductivity of 10^{-6} – $10^{-5} \text{ S cm}^{-1}$ at $25 \text{ }^\circ\text{C}$ [172]. Meanwhile cubic Na_3PS_4 (*c*- Na_3PS_4) was proposed by Hayashi et al. [173] with an enhanced ionic conductivity of $2 \times 10^{-4} \text{ S cm}^{-1}$ at room temperature. The *c*- Na_3PS_4 could be obtained by employing mechanochemical methods and consequent heat treatment at $270 \text{ }^\circ\text{C}$ [174]. This *c*- Na_3PS_4 prepared at low temperatures exhibited a high ionic conductivity of $4.6 \times 10^{-4} \text{ S cm}^{-1}$.

Wenzel et al. [105] presented interfacial reactivity benchmarking of the sodium ion conductor Na_3PS_4 , as demonstrated in Fig. 3a: a strong impedance increase was observed and the overall resistance was approximately doubled. The CV results show great changes in slope within the initial a few hours, which indicates a sharp increase in polarization resistance as a result of the reaction at the interface. Moreover, Fig. 3b shows that the interface resistance increases almost linearly due to the formation of interfacial reaction products.

Chu et al. [175] predicted the phase stability of $\text{Na}_{3-x}\text{PS}_{4-x}\text{Cl}_x$. Fig. 3c illustrates the electrochemical decomposition products of doped Na_3PS_4 compounds. The *Y*-axis refers to Na uptake per formula unit. With regard to the inclusion of chlorides, $\text{Na}_{3-x}\text{PS}_{4-x}\text{Cl}_x$ is stable against sodium metal till a potential of 2.4 V versus Na/Na^+ , above which the formation of $\text{NaPS}_3 + \text{S} + \text{NaCl}$ is pre-

dicted to occur. However, if the operating voltage is within 2.4 V, the predicted phase equilibrium at the charged cathode–solid-state electrolyte interface retains $t\text{-Na}_3\text{PS}_4 + \text{NaCl}$ as the primary component [175]. After symmetric Na/SSE/Na cell cycling, with XPS, the interface between Na and SSEs has been observed to form Na_2S and Na_3P for Na_3PS_4 and Na_2S , Na_3P and NaCl for $\text{Na}_{3-x}\text{PS}_{4-x}\text{Cl}_x$ (Fig. 3d) [176]. This interface degradation in the presence of Na metal, where some of the decomposition products exhibit low band gap and are not pure electronic insulators, could form harmful MCI and badly affect the electrochemical cell performance. Note that Na_3P is actually a semiconductor with a small band gap of 0.4 eV [177] and thus exhibits mixed conduction, in contrast to the ionically conductive but electronically insulating lithium counterpart (*i.e.*, Li_3P). Note that, due to the presence of non-negligible oxygen contamination in the phosphosulfide Li-counterpart ($\text{Li}_2\text{S-P}_2\text{S}_5$), Wood et al. unveiled by using operando X-ray photoelectron spectroscopic technique that the Li metal/electrolyte interface contains trace Li^+ , inhibiting Li_3PO_4 and Li_2O phases [178]. Such presence in Na_3PS_4 and the potential impact on the ionic conductivity across the interface is yet to be studied. Any phosphate or thiophosphate Na solid-state electrolyte that can be reduced to Na_3P upon contacting with Na metal, should therefore be avoided pairing up with Na metal. However, on halogen substitution of phosphorous, formation of NaX ($X = \text{F}, \text{Cl}, \text{Br}, \text{I}$) could provide passivating quality. This could improve cell performance and slow the kinetics of degradation, owing to the reduction of the mole fraction of mixed conducting phase, such as Na_3P .

Bo et al. [179] have deduced structure-dependent ionic conduction properties by partially substituting S with Se that can result in $\text{Na}_3\text{PS}_x\text{Se}_{4-x}$. The addition of Se led to a crystal structure transition from tetragonal to cubic system, with a concomitant increase in the ionic conductivity and reduction in the activation energies. Na_3PSe_4 is acquired by completely substituting S with Se [180]. Tian et al. [181] examined the compatibility issues between sodium and Na_3PSe_4 , which led to the observation that the calculated stability window from 1.8 to 2.15 V is narrower than the experimentally estimated one up to 2.6 V from CV measurements. However, a low-current (close to equilibrium) galvanostatic cycling of Na_3PSe_4 as an electrode shows a more consistent result with their theoretical prediction. Na_3PSe_4 was observed to decompose when charged to 2.5 V or discharged below 0.5 V, with respect to the oxidation and reduction peaks of Na_3PSe_4 (Fig. 4a). When the cell is charged at 2.5 V, new Se peaks emerge from *ex-situ* X-ray diffraction (XRD) measurements as shown in Fig. 4b. This indicates that Na_3PSe_4 is stable only up to 2.33 V. On the other hand, during the discharge process, a small capacity is delivered in the voltage slope region of 1.25–2.10 V. This voltage was ascribed to Se obtained from the preparation process since the reduction potential of Se is approximately 2 V [182]. This implies that the cathodic stability limit of Na_3PSe_4 could be assigned to be 1.25 V and the overall electrochemical stability window of Na_3PSe_4 via the charge/discharge method was determined to be 1.25–2.33 V. Meanwhile, a symmetric Na/ Na_3PSe_4 /Na cell that was cycled at a current density of 0.1–0.2 mA cm^{-2} short circuited after approximately 12 h of cycling. XRD analyses of the electrolyte after cycling suggest that Na_3PSe_4 fully decomposed into amorphous components.

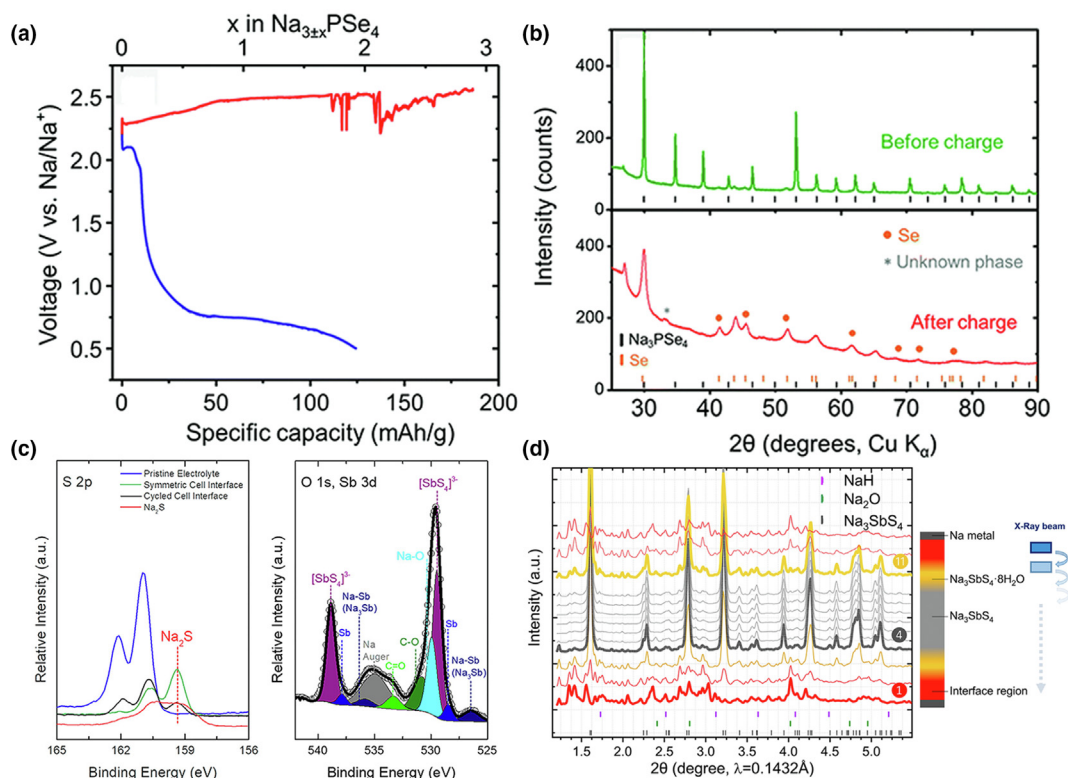
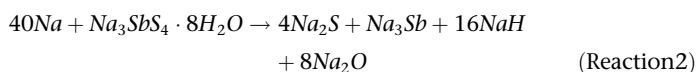
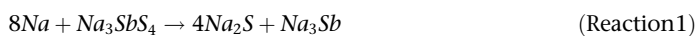


FIGURE 4

(a) Electrochemical cycling of Na_3PSe_4 cathodes (mixed with carbon) at the current density of 2.404 mA g^{-1} . (b) *Ex-situ* XRD patterns of Na_3PSe_4 before and after charge. Reproduced from Ref. [181] with permission, Copyright 2017, Royal Society of Chemistry. (c) XPS region scan of Na_3SbS_4 interface after symmetric cell cycling. Reproduced from Ref. [176] with permission, Copyright 2018, American Chemical Society. (d) SXR depth profiling of as-air exposure symmetric cells along the vertical axis. The color of each XRD pattern corresponds to one layer of the schematic illustration. Reproduced from Ref. [118] with permission, Copyright 2019, Elsevier.

Replacing P^{5+} with Sb^{5+} could acquire a superionic conductor in Na_3SbS_4 [183,184], which has been touted as a promising solid-state electrolyte for sodium ion batteries owing to its good air stability. This cubic material could be synthesized by dehydration [183] or solution process [185,186]. Na_3SbS_4 undergoes a chemical reaction (Reaction 1) against sodium metal forming Na_3Sb and Na_2S at the interface, as verified from XPS (Fig. 4c). One of the reaction products, Na_3Sb , is a small band gap material, making the interface an MCI [176]. Tian et al. [118] introduced a reverse interface engineering route to protect the Na/ Na_3SbS_4 interface. With the help of first-principles screening, NaH and Na_2O were predicted to be thermodynamically stable upon the contact with Na metal [159]. Hence, they partially hydrated the Na_3SbS_4 interface to form $\text{Na}_3\text{SbS}_4 \cdot 8\text{H}_2\text{O}$, which, once in contact with Na metal, undergoes another chemical process (Reaction 2) producing passivating products such as NaH and Na_2O . The reaction products were characterized with the help of synchrotron X-ray diffraction (SXR) depth profiling, and the results are presented in Fig. 4d. Comparing the two reactions,



one can find that the fraction of the electron conducting phase dramatically decreases from 20 mol% to 3 mol%, resulting in greatly improved interface stability with the formation of a more passivating 'SEI' phase. Solution-based synthesis could be used to obtain Na_3SbS_4 and its derivative, $\text{NaI} \cdot \text{Na}_3\text{SbS}_4$, by fully dissolving in protic solvents such as MeOH or water and avoiding any secondary reactions [187]. The latter compound exhibited an ionic conductivity in the range of 0.74 mS cm^{-1} .

High-throughput screening is an efficient and convenient method to filtrate the potential existence of materials in a disparate structure. Richards et al. [188] predicted the formation of LGPS-structure-type $\text{Na}_{10}\text{SnP}_2\text{S}_{12}$, which exhibits $P-4m2$ space group, and the structure consists of three symmetrically distinct chains of cations oriented parallel to the c-axis, exhibiting 1D ionic conduction, by using *ab initio* molecular dynamics (AIMD) simulations. The as-synthesized tetragonal $\text{Na}_{10}\text{SnP}_2\text{S}_{12}$ shows a conductivity of 0.4 mS cm^{-1} with an activation energy of 0.356 eV , which is in remarkable agreement with AIMD results. Richards et al. [188] also continued to study the stability limits of $\text{Na}_{10}\text{SnP}_2\text{S}_{12}$. From the Na-Sn-P-S phase diagram (Fig. 5a), one could see that the $\text{Na}_{10}\text{SnP}_2\text{S}_{12}$ phase is metastable at 0 K. The authors considered the potentials at which the ground-state materials' (Na_4SnS_4 or Na_3PS_4) equilibrium becomes unstable, making $\text{Na}_{10}\text{SnP}_2\text{S}_{12}$ unstable. Above 1.82 V , Na_4SnS_4 decomposes to S and Na_2SnS_3 versus Na metal, and below 1.25 V , phosphorus is partially reduced to form Na_2PS_3 . Hence,

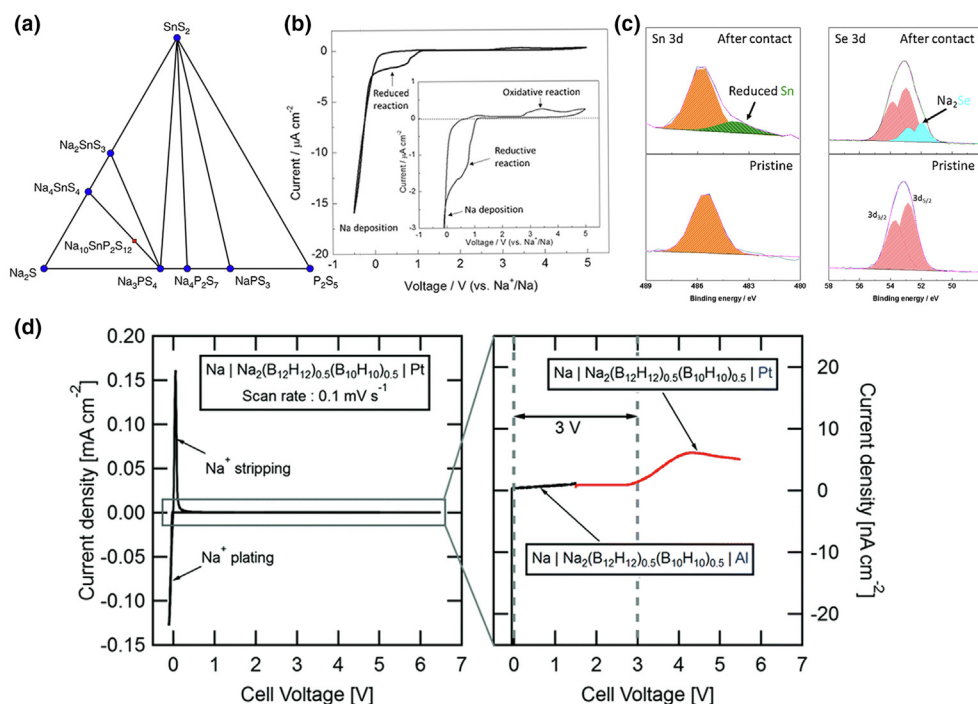


FIGURE 5

(a) Pseudo-ternary 0 K Na-Sn-P-S phase diagram with location of $\text{Na}_{10}\text{SnP}_2\text{S}_{12}$. Stable phases are marked with blue dots. Reproduced from Ref. [188] with permission, Copyright 2016, Springer Nature. (b) CV tests of $\text{Na}/\text{Na}_{11}\text{Sn}_2\text{PSe}_{12}$ pellets before and after contact with sodium metal. Reproduced from Ref. [194] with permission, Copyright 2019, Elsevier. (c) XPS profile Sn 3d and Se 3d of $\text{Na}_{11}\text{Sn}_2\text{PSe}_{12}$ pellets before and after contact with sodium metal. Reproduced from Ref. [194] with permission, Copyright 2019, Elsevier. (d) Room temperature CV profiles of the $\text{Na}|\text{Na}_2(\text{B}_{12}\text{H}_{12})_{0.5}(\text{B}_{10}\text{H}_{10})_{0.5}|\text{Pt}$ cell from 0.5 to 6.5 V with a scan rate of 0.1 mV s^{-1} as well as $\text{Na}|\text{Na}_2(\text{B}_{12}\text{H}_{12})_{0.5}(\text{B}_{10}\text{H}_{10})_{0.5}|\text{Al}$ and $\text{Na}|\text{Na}_2(\text{B}_{12}\text{H}_{12})_{0.5}(\text{B}_{10}\text{H}_{10})_{0.5}|\text{Pt}$ cells between 0.5 and 5.5 V showing the oxidative (red) and reductive (black) stability of the electrolyte. Reproduced from Ref. [195] with permission, Copyright 2017, Royal Society of Chemistry.

the electrochemical stability window of $\text{Na}_{10}\text{SnP}_2\text{S}_{12}$ is predicted to be 1.25–1.82 V.

Recent reports on the aliovalent substitution of Sb^{5+} sites in Na_3SbS_4 by Sn^{4+} have resulted in a new class of sodium ion conducting solid electrolytes associated with a general formula, $\text{Na}_{4-x}\text{Sn}_{1-x}\text{Sb}_x\text{S}_4$ ($0.02 \leq x \leq 0.33$) [189]. With an upper limit of Sb^{5+} substitution, the stoichiometric system of $\text{Na}_{11}\text{Sn}_2\text{SbS}_{12}$ exhibits fairly good ionic conductivity (around 0.2 mS cm^{-1}). Also, the electrochemical stability window for the composition of $\text{Na}_{11.25}\text{Sn}_{2.25}\text{Sb}_{0.75}\text{S}_{12}$ was estimated to be in the range of 0.44–4.5 V (vs Na/Na^+) [189]. In addition, these compounds retain ionic conduction even after several hours of exposure to air. Isovalent substitution of Sb^{5+} with P^{5+} or S^{2-} with Se^{2-} results in chalcogenide-based solid-state electrolytes $\text{Na}_{11}\text{Sn}_2\text{PS}_{12}$ [190] and $\text{Na}_{11}\text{Sn}_2\text{PSe}_{12}$ [191] with improved ionic conductivities (1 and 4 mS cm^{-1} , respectively). $\text{Na}_{11}\text{Sn}_2\text{PS}_{12}$ comprises characteristic 3D chessboard frameworks of SnS_4 and PS_4 tetrahedra that delimit wide Na^+ channels along the c axis and within the ab planes. Zhang et al. [192] suggested that $\text{Na}_{11}\text{Sn}_2\text{PS}_{12}$ is oxidatively stable up to 5 V by CV studies. As for reduction stability, from XPS analyses of the sample after the CV scan down to -0.5 V , Na_2S and Sn were observed to form at the interface [193]. This interface can be, hence, categorized as a harmful MCI. On the other hand, the electrochemical stability window of $\text{Na}/\text{Na}_{11}\text{Sn}_2\text{PSe}_{12}$ obtained from the CV test (Fig. 5b) was in the range of 1.22–2.65 V. Furthermore, below 1.22 V and above 2.65 V, $\text{Na}_{11}\text{Sn}_2\text{PSe}_{12}$ exhibits reductive and oxidative reactions,

respectively [194]. The decomposition products at the $\text{Na}/\text{Na}_{11}\text{Sn}_2\text{PSe}_{12}$ interface are identified to be Sn and Na_2Se from XPS (Fig. 5c) rendering the interface an MCI. The evolution of toxic H_2Se gas can be avoided in these compounds unlike other sulfides that contain phosphorus.

Complex hydrides

The sodium ion conduction in the complex hydrides was reported for the first time in 2012 [196]. Amongst them, the borohydride type SSEs showed great potential as replacement for liquid electrolytes. Udovic et al. [196] opened up the research on complex hydrides as the sodium solid-state electrolytes. They synthesized two kinds of SSEs: NaAlH_4 and Na_3AlH_6 that exhibited ionic conductivities of 2.1×10^{-10} and $6.4 \times 10^{-4} \text{ S cm}^{-1}$ at room temperature, respectively. As predicted by density functional theory (DFT), NaAlH_4 and Na_3AlH_6 are intrinsic electronic insulators and fast ion conductors at high temperature [197].

Following their design, Duchêne et al. [198] presented another kind of complex hydride superionic conductors: disordered sodium decahydro-closo-decaborate $\text{Na}_2\text{B}_{10}\text{H}_{10}$, showing a pseudo-face-centered-cubic (FCC) framework. $\text{Na}_2\text{B}_{10}\text{H}_{10}$ exhibits a monoclinic phase (space group $P2_1/c$, $a = 6.65 \text{ \AA}$, $b = 13.13 \text{ \AA}$, $c = 11.8 \text{ \AA}$, with $\beta = 120.20^\circ$). $\text{Na}_2\text{B}_{10}\text{H}_{10}$ transformed from order to disorder phase at 375 K, and the disordered $\text{Na}_2\text{B}_{10}\text{H}_{10}$ exhibited high ionic conductivity of 0.01 S cm^{-1} and low activation energy of 0.19 eV. Chen and co-workers [199] drew a

conclusion that $\text{Na}_2\text{B}_{10}\text{H}_{10}$ is a ductile material with low polycrystalline bulk modulus, shear modulus and Young's modulus.

The dodeca/deca-borate mixture pseudo-binary complex hydride, which exhibits high ionic conductivity of the order of $10^{-4} \text{ S cm}^{-1}$ at room temperature, has been proved to be stable against sodium metal [200]. Duchêne et al. [195] spearheaded the research on the pseudo-binary complex-hydride-based sodium ion superionic conductors. They believed that the stability window of the closo-borate electrolytes was overestimated based on CVs of the $\text{Na}|\text{Na}_2(\text{B}_{12}\text{H}_{12})_{0.5}(\text{B}_{10}\text{H}_{10})_{0.5}|\text{Pt}$ cell with a value of 0–6 V (Fig. 5d). The overestimation could have been caused by: (a) the very small oxidation currents that could only be detected by the high-resolution detector with pA resolution or (b) an artificial increase in the contact area between the electrolyte and the working electrode. In practice, they showed that $\text{Na}_2(\text{B}_{12}\text{H}_{12})_{0.5}(\text{B}_{10}\text{H}_{10})_{0.5}$ could only offer an electrochemical stability window of 3 V, beyond which small decomposition current of less than 10 nA cm^{-2} was observed (Fig. 5d). Nevertheless, promising high-performance full cells were demonstrated based on these closo-borate electrolytes [201].

Perovskites

Oxide-based perovskite solid-state electrolytes exhibiting high oxide ionic conductivity of $\sim 10^{-3} \text{ S cm}^{-1}$ at room temperature have been comprehensively used as solid oxide fuel cells (SOFCs), oxygen sensors and air separation membranes [202]. Recently, high lithium/sodium ion conductivities were also reported in these classes of materials.

The ionic conductivities of $\text{Na}_{0.33}\text{La}_{0.55}\text{ZrO}_3$ (NLZO) and Sr substituted $\text{Na}_{1/3}\text{La}_{1/3}\text{Sr}_{1/3}\text{ZrO}_3$, which are indexed to an orthorhombic crystal structure, were found to be 6.89×10^{-7} and $1.025 \times 10^{-5} \text{ S cm}^{-1}$ at room temperature, respectively. Unlike the perovskite type lithium lanthanum titanate (LLTO), which has the easily reducible titanium ion, the sodium perovskite type SSEs of $\text{Na}_{0.33}\text{La}_{0.55}\text{ZrO}_3$ (NLZO) and Sr substituted $\text{Na}_{1/3}\text{La}_{1/3}\text{Sr}_{1/3}\text{ZrO}_3$ contain more stable elements of La, Zr and Sr and may possess higher chemical stability with sodium metal [203].

Antiperovskites

Since the discovery of antiperovskite $\text{Li}_3\text{OCl}_{1-x}\text{Br}_x$ [204] with high lithium ion conduction and good electrochemical stability window, search for sodium-based analogs of the antiperovskite-type solid-state electrolytes (with a chemical composition of $\text{Na}_3\text{-OX}$, where $X = \text{Cl, Br, I}$ and BH_4), crystallizing into a cubic structure (space group $Pm\bar{3}m$, $a = 4.564 \text{ \AA}$), with high ionic conductivity has gained much attraction over the recent years.

Electronic structure of Na_3OCl and Na_3OBr estimated with full potential-linearized augmented plane wave (FP-LAPW) method demonstrates that these compounds are direct band gap insulators [205]. Elastic constants from DFT calculations reveal that Na_3OCl is mechanically stable, but Na_3OBr is brittle in nature [206].

Some Li-nonmetal binary phases formed between the lithium anode and SSEs have been proved to be an effective passivate layers against lithium [207], which are similar in nature to sodium as well. The sodium antiperovskite type SSEs consist of sodium, oxygen, and halogen/rotational clusters (e.g., BH_4). It is also

expected to form ionically conducting but electronically insulating NaX ($X = \text{halogen}$) when the SSE is in contact with sodium anodes [111]. Unfortunately, the antiperovskite SSEs discovered so far were estimated to be stable only for a window of 0–1.8 V.

Choosing the ideal solid-state electrolyte

In this section, we will make a summative comparison of the SSEs discussed in the above section with respect to their ionic conductivity, electronic conductivity, electrochemical stability window, mechanical strength and resistivity with sodium, and further address various common issues associated with each class of inorganic solid-state electrolytes. By considering the average values of various properties for different classes of SSEs, we create a radar plot highlighting the advantages and disadvantages of each class of materials, as shown in Fig. 6. Detailed information is shown in Table 1. Finally, this section will also address the grain boundary effect that predominantly exists among oxide-based solid-state electrolytes.

Ionic conductivity

To be efficiently functioning as a solid-state electrolyte, the ionic conductivity of the material is generally the top priority among other properties. Chalcogenide SSEs including sulfide-based, selenium-based and their mixed compounds; NASICON; and complex hydrides all exhibit high ionic conductivities in the range of 10^{-4} – $10^{-3} \text{ S cm}^{-1}$ at room temperature. However, among all the sodium-based inorganic solid-state electrolytes, sodium β -alumina possesses one of the highest ionic conductivities at room temperature, which lies in the range of $10^{-2} \text{ S cm}^{-1}$ [154]. These conductivity values are comparable to those of the sodium ion-based liquid electrolytes. The perovskite and antiperovskite SSEs exhibit non-ideal ionic conductivities that are much less than those of other types of SSEs by 4 or 5 orders of magnitude. However with the introduction of rotational cluster anion BH_4^- in Na_3OBH_4 , the ionic conductivity can be improved to a much higher value of $4.4 \times 10^{-3} \text{ S cm}^{-1}$ at room temperature [217]. There is no doubt that ionic conductivity is an important and fundamental criterion of an ideal solid-state electrolyte, but as discussed throughout this review, this is not the only factor controlling battery performance.

Electronic conductivity

The electronic conductivity in solid-state electrolytes has recently emerged as one of the root causes for the formation of dendrites [221]. This concept could also be extended to electronic conductivity induced by sodium dendrite growth within the sodium-based SSEs. It is understood that electronic conductivity is a decisive factor that controls the critical current density that in turn brings down the performance of the battery. Therefore, we emphasize the importance of electronic conductivity of the solid-state electrolyte in this review. As for sodium β -alumina [105], it is an electronic insulator with an electronic conductivity of $6 \times 10^{-12} \text{ S cm}^{-1}$. When it comes to other types of sodium-based SSEs, they are considered to be pure ionic conductors only when the Na^+ ion transfer number (equal to ionic conductivity divided by the total conductivity from both ionic and electronic conductivities) is approximate to 1. It is advisable to ignore the effect of electronic conductivity when it is lower than the ionic

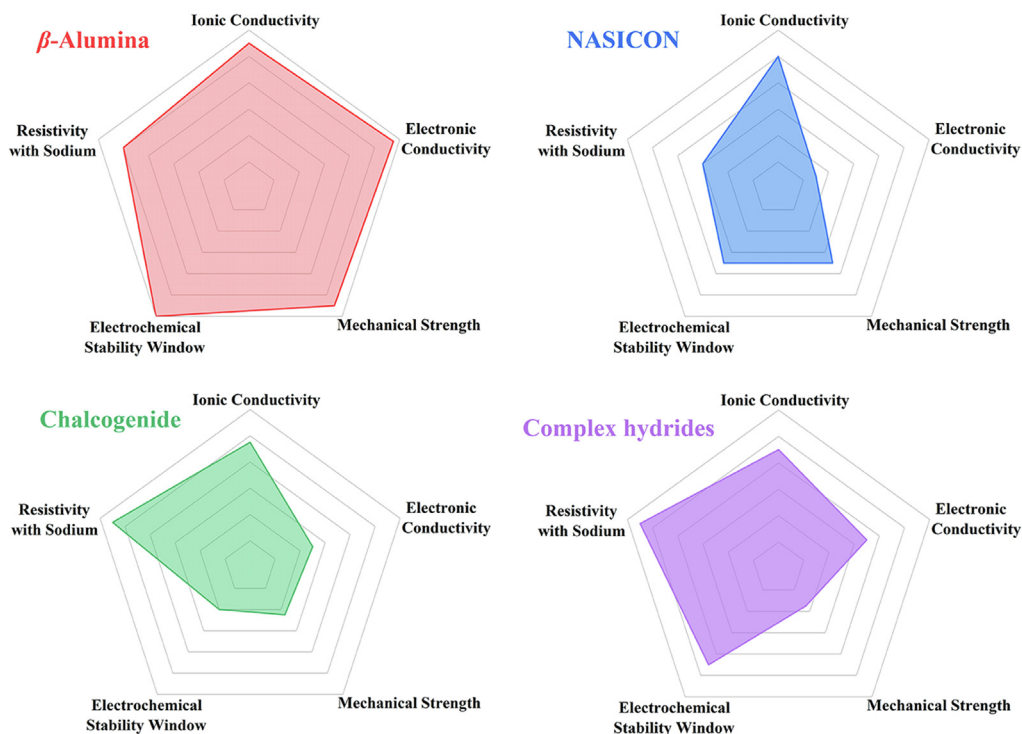


FIGURE 6

Radar plots of the various physical and chemical properties of solid-state electrolytes indicating their relative performances.

conductivity by at least 4 orders of magnitude. Many of the fast ion conductors meet this condition. It should be noted that Han et al. reports that the electronic conductivity of LLZO and LPS is only at 10^{-8} and 10^{-9} S cm^{-1} , respectively and, yet, plays an important role in the growth of lithium dendrites. In comparison, the electronic conductivity of NASICON [222] was found to be the highest at 10^{-7} S cm^{-1} at room temperature. Chalcogenide [105,176,180,186,192], complex hydride [196] and perovskite [203] SSEs possess slightly lower values of electronic conductivity in the range of 10^{-8} to 10^{-9} S cm^{-1} , of which the electronic conductivity of complex hydrides is as low as 4.9×10^{-9} S cm^{-1} . Moreover, only very few papers have focused on the sodium antiperovskite SSEs, with a notable mention that their electronic conductivity is negligible [223].

Mechanical strength

Mechanical strength of the material is another crucial parameter to evaluate the solid-state electrolyte's resistance to deformation from external pressure. Young's modulus and shear modulus are the two main elastic modulus parameters to compare among the SSEs. Young's modulus is used to describe the material's ability to resist deformation. Shear modulus is the ratio of shear stress to shear strain where shear stress is within the limit of elastic deformation. As such, it represents the material's resistance to shear deformation. Ideally, the shear modulus of the solid-state electrolyte is preferred to exhibit approximately twice or higher than the shear modulus of sodium metal (3.3 GPa). This could serve as suggestion for suitable solid-state electrolytes [224]. The solid-state electrolytes designed based on oxide compounds possess good mechanical strength: sodium β -alumina has a considerably high Young's modulus of 200 GPa [225] and a shear modulus

and 35 GPa [226]; NASICON exhibits a Young's modulus of 75 GPa and a shear modulus of 44.3 GPa [225]; 200 GPa and 55 GPa for perovskite SSEs; and those for antiperovskite SSEs are about 61 GPa and 20.9 GPa [227]. The shear modulus of all these materials satisfies the conditions of larger than twice that of sodium metal. But it is also noteworthy that a higher mechanical strength could mean strenuous processing conditions. On the contrary, chalcogenide and complex-hydride-based SSEs possess lower mechanical strength: the range of chalcogenide SSEs' Young's modulus is 18–25 GPa [228] and shear modulus of 5–6 GPa for glass sulfides [229] and varies from a few GPa to higher than 10 GPa for ceramics depending on the composition [114]; the Young's modulus and shear modulus of complex hydrides are 12.75 and 5.5 GPa, respectively [199]. Therefore, one has to be more careful when judging if a chalcogenide or complex hydride satisfies Monroe's criterion.

Electrochemical stability window

Electrochemical stability window has been obtained by both experimental methods and theoretical simulations. However, the two methods can yield substantially different results in some cases. Tang et al. [230] and Lacivita et al. [159] summarized the electrochemical stability window of Na solid-state electrolyte candidates through *ab-initio* investigations, and the oxidation and reduction potentials are also listed in the charts (Fig. 7a, b). It is to be noted that the *ab-initio* calculations were made at 0 K. Sodium β -alumina is stable against sodium metal even at high temperatures. By CV tests of the Ag|NASICON|Na cell, researchers found NASICON stable against sodium in the range of 1.75–5.0 V [209]. However, a NASICON type solid-state electrolyte is theoretically predicted to be stable against sodium at

TABLE 1

Electrochemical properties for sodium-based SSEs.

| Type | Chemical Formula | Ionic Conductivity (S cm ⁻¹) | Ea (eV) | Electronic Conductivity (S cm ⁻¹) | Electrochemical Window (V) | Predicted Window (V) | Shear Modulus (GPa) | Young's Modulus (GPa) | Interfacial Resistance | Wettability | Reference |
|------------------|--|--|---------|---|----------------------------|----------------------|-----------------------|------------------------|------------------------|-------------|-----------|
| β -Alumina | β -Al ₂ O ₃ | 1.4 × 10 ⁻² (25 °C) | 0.16 | 6 × 10 ⁻¹² | – | – | 35 | 200 | 120 Ω | × | [154] |
| | β'' -Al ₂ O ₃ | 1 × 10 ⁻¹ (25 °C) | 0.20 | – | – | – | – | – | – | – | [105,208] |
| NASICON | Na ₃ Zr ₂ Si ₂ PO ₁₂ | 1.13 × 10 ⁻³ (20 °C) | 0.32 | 2.35 × 10 ⁻⁷ | 1.75–5.0 | 1.1–3.5 | 44 | 75 | 14.25 kΩ | × | [209,210] |
| | Na _{3,4} Zr _{1,8} Zn _{0,2} Si ₂ PO ₁₂ | 1.44 × 10 ⁻³ (25 °C) | 0.28 | – | – | – | – | – | – | – | [211] |
| | Na ₃ La(PO ₄) ₃ | 1.10 × 10 ⁻³ (25 °C) | – | – | – | – | – | – | – | – | [212] |
| | Na _{3,4} Zr _{1,6} Sc _{0,4} Si ₂ PO ₁₂ | 4 × 10 ⁻³ (25 °C) | 0.26 | – | 0.3–6 | – | – | – | – | – | [213] |
| Chalcogenides | Na ₃ PS ₄ | 2 × 10 ⁻⁴ (25 °C) | 0.28 | 8.9 × 10 ⁻⁸ | 0–5 | 1.39–2.45 | 5–10 | 18–25 | 60 Ω | ✓ | [105,173] |
| | Na _{2,73} Ca _{0,135} PS ₄ | 9.4 × 10 ⁻⁴ (25 °C) | 0.49 | – | – | – | – | – | – | – | [214] |
| | Na _{2,9375} PS _{3,9375} Cl _{0,0625} | 1.14 × 10 ⁻³ (25 °C) | 0.25 | – | 0–2.4 | – | – | – | – | – | [175] |
| | Na ₃ SbS ₄ | 1.05 × 10 ⁻³ (25 °C) | 0.22 | 1.9 × 10 ⁻¹⁰ | 0.5–5 | 1.83–1.90 | – | – | 40 Ω cm ² | – | [183] |
| | Na _{2,88} Sb _{0,88} W _{0,12} S ₄ | 3.2 × 10 ⁻² (25 °C) | 0.18 | – | – | – | – | – | – | – | [68] |
| | 0.1NaI-0.9Na ₃ SbS ₄ | 7.4 × 10 ⁻⁴ (30 °C) | 0.30 | – | – | – | – | – | – | – | [187] |
| | Na ₃ PSe ₄ | 1.16 × 10 ⁻³ (25 °C) | 0.21 | – | – | – | 1.57–1.87 | – | – | – | [180] |
| | Na ₃ SbSe ₄ | 8.5 × 10 ⁻⁴ (25 °C) | 0.19 | 4.24 × 10 ⁻⁸ | – | – | – | – | – | – | [215] |
| | Na ₁₁ Sn ₂ PS ₁₂ | 1.4 × 10 ⁻³ (25 °C) | 0.25 | 7.17 × 10 ⁻⁹ | 1.25–5 | – | 1.37–2.23 | – | – | – | [192] |
| | Na ₁₁ Sn ₂ SbS ₁₂ | 5.9 × 10 ⁻⁴ (25 °C) | 0.34 | – | 0.44–4.5 | – | – | – | – | – | [190] |
| | Na ₁₁ Sn ₂ PSe ₁₂ | 2.15 × 10 ⁻³ (30 °C) | 0.28 | 1.87 × 10 ⁻⁷ | 1.22–2.65 | – | – | – | – | – | [194] |
| | 94Na ₃ PS ₄ ·6Na ₄ SiS ₄ | 7.4 × 10 ⁻⁴ (25 °C) | – | – | – | 0–5 | – | – | – | – | [216] |
| Type | Chemical Formula | Ionic Conductivity (S cm ⁻¹) | Ea (eV) | Electronic Conductivity (S cm ⁻¹) | Electrochemical Window (V) | Shear Modulus (GPa) | Young's Modulus (GPa) | Interfacial Resistance | Wettability | Reference | |
| Complex hydrides | NaAlH ₄ | 2.1 × 10 ⁻¹⁰ (25 °C) | 0.79 | – | – | 6 M | 12.75 | 2 × 10 ⁶ Ω | ✓ | [196] | |
| | Na ₃ AlH ₆ | 6.4 × 10 ⁻⁷ (25 °C) | 0.62 | – | – | – | – | 9 × 10 ³ Ω | – | [196] | |
| | Na ₂ B ₁₀ H ₁₀ | 1 × 10 ⁻² (110 °C) | 0.19 | 4.9 × 10 ⁻⁹ | 0–5 | – | – | – | – | [198] | |

(continued on next page)

TABLE 1 (CONTINUED)

| Type | Chemical Formula | Ionic Conductivity ($S\text{ cm}^{-1}$) | Ea (eV) | Electronic Conductivity ($S\text{ cm}^{-1}$) | Electrochemical Window (V) | Shear Modulus (GPa) | Young's Modulus (GPa) | Interfacial Resistance | Wettability | Reference |
|-----------------|---|---|---------|--|----------------------------|---------------------|-----------------------|------------------------|-------------|-----------|
| Perovskites | $\text{Na}_2(\text{B}_{12}\text{H}_{12})_{0.5}(\text{B}_{10}\text{H}_{10})_{0.5}$ | 9×10^{-4} (20 °C) | 0.4 | - | 0–3 | - | - | - | - | [195] |
| | $\text{Na}_2(\text{B}_{12}\text{H}_{12})_{0.75}(\text{B}_{10}\text{H}_{10})_{0.25}$ | 3.2×10^{-3} (30 °C) | 0.56 | - | 0–5 | - | - | - | - | [200] |
| | $\text{Na}_{1/3}\text{La}_{1/3}\text{Sr}_{1/3}\text{ZrO}_3$ | 1.025×10^{-5} (25 °C) | - | 8.17×10^{-8} | - | 55 | 200 | - | × | [203] |
| Antiperovskites | $\text{Na}_{0.33}\text{La}_{0.55}\text{ZrO}_3$ | 6.89×10^{-7} (25 °C) | - | - | - | - | - | - | - | [203] |
| | Na_3OBH_4 | 4.4×10^{-3} (25 °C) | 0.25 | - | - | 21 | 61 | - | ✓ | [217] |
| SSEs | Na_3OBr | 9.02×10^{-7} (180 °C) | 0.84 | - | 0–1.6 | - | - | - | - | [218] |
| | Na_4O_2 | 2.47×10^{-4} (230 °C) | 0.65 | - | 0–1.5 | - | - | - | - | [219] |
| | $\text{Na}_3\text{OBr}_{0.60.4}$ | 4.30×10^{-4} (200 °C) | 0.63 | - | - | - | - | - | - | [220] |
| | $\text{Na}_{2.9}\text{O}_{0.05}\text{Sr}_{0.05}\text{OBr}_{0.60.4}$ | 9.50×10^{-4} (180 °C) | 0.62 | - | - | - | - | - | - | [220] |

1.13–3.35 V [230]. Meanwhile, the electrochemical stability window of chalcogenide SSEs was estimated to be fairly narrow because they are easily reduced by alkali metals. The predicted values were only 1.16–2.49 V [230] and 1.39–2.45 V [159] for Na_3PS_4 ; 1.54–2.35 V [230] and 1.83–1.90 V [159] for Na_3SbS_4 ; and 1.37–2.23 V [159] for $\text{Na}_{11}\text{Sn}_2\text{PS}_{12}$. However, CV tests of the symmetric cell showed that Na_3PS_4 , Na_3SbS_4 and $\text{Na}_{11}\text{Sn}_2\text{PS}_{12}$ were stable up in 0–5 [231], 0.5–5 [183] and 1.25–5 V [192], respectively. Complex hydride SSEs with the constitution of unary or binary $\text{B}_{10}\text{H}_{10}^{2-}$ and $\text{B}_{12}\text{H}_{12}^{2-}$ possess good electrochemical stability against sodium in the range of 0–3 V [195] as demonstrated through CV tests. DFT investigations predicted an overall range from 0 V up to 3.5 V [159] for complex hydrides. The antiperovskite SSEs were novel and only one theoretical electrochemical stability window was reported to be within 0–1.8 V [159].

The significant difference between computation and experiment in voltage stability for NASICON and chalcogenide SSEs may arise from multiple reasons. First, there might be artifacts in the experimental methods. Most previous CV tests have limited precision, as discussed above in Fig. 5d, so the weak (electro)-chemical reactions may be ignored by either the instrumental detection sensitivity or simply due to the relatively large scale in the measurement and/or figure plot set by the researcher, leading to a report of wider voltage stability than the exact thermodynamic prediction. Two approaches could address this issue: one, by improving the detection sensitivity and the other, by amplifying the signal of the weak reaction. Second, given the limited electronic conductivity of the SSEs and finite contact between the solid-state electrolyte and sodium anode, the electrochemical reaction depending on the electron transfer may not proceed completely. Mixing the SSEs with electron conductors, such as carbon black, can significantly enhance the reaction response rate and hence give a more precise electrochemical stability window. Third, most computations did not consider the mechano-electrochemical interactions that can widen the voltage stability window for solid-state electrolytes [115]. The effect is predicted to be prominent for electrolytes with high reaction strains, like chalcogenide families [116,232]. For example, the standard thermodynamic voltage window for $\text{Li}_{10}\text{GeP}_2\text{S}_{12}$ and Li-Si-P-S electrolytes of 1.7–2.1 V was predicted to be widened by such effect to around 1–4 V. Similar effect may exist for Na chalcogenides.

Sodium wettability

Sodium wettability can be reflected by interfacial resistivity. Interfacial resistivity is the occurrence of a finite value of resistance at the interface between the solid-state electrolyte and sodium, as a result of occurrence of decomposition products from chemical reactions or the improper contact between the phases involved. This influences the specific capacity and cyclic performance of solid-state batteries [159]. Interpreting from the previous sections, the interfacial resistances are predominantly affected by the lack of proper contact in the case of oxides and hydrides, whereas chalcogenides are affected by their high reactivity. In addition to the low interfacial resistance (120 Ω) between β -alumina and sodium metal, β -alumina was found to be fairly stable against sodium as there was no significant degra-

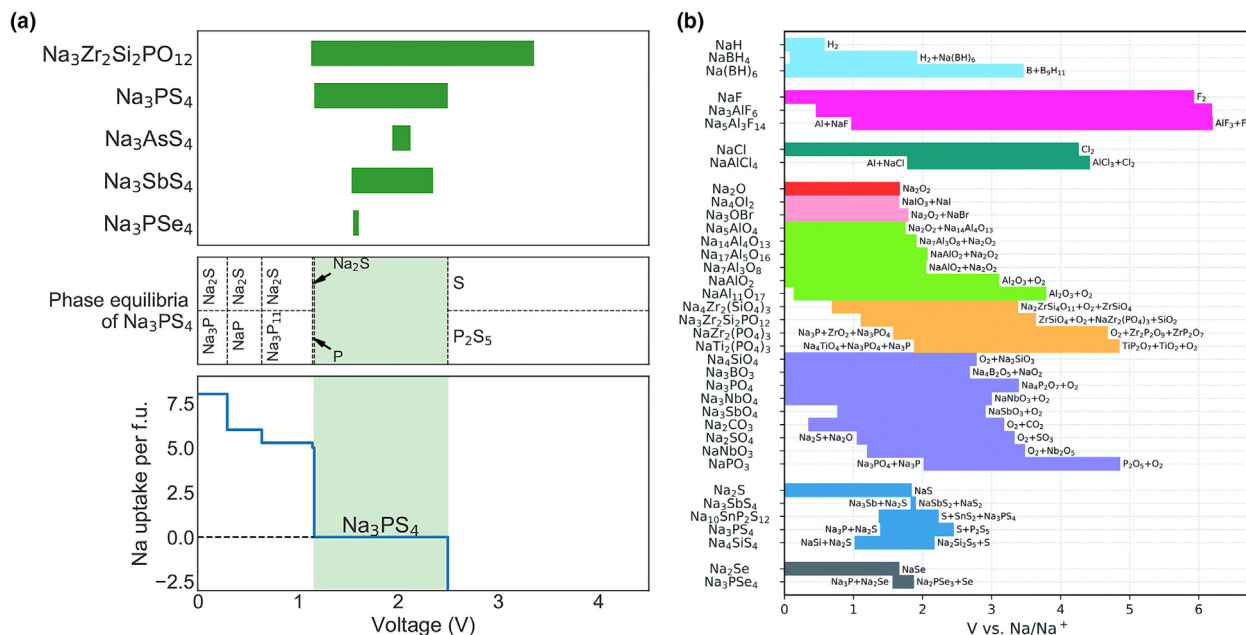


FIGURE 7

(a) Predicted electrochemical stability window of solid-state electrolytes (top). Predicted phase equilibria (middle) and Na uptake per formula unit (bottom) of Na₃PS₄ vs voltage (V). Reproduced from Ref. [230] with permission, Copyright 2018, American Chemical Society. (b) Calculated electrochemical stability windows of sodium-based solid-state electrolyte candidates. Reproduced from Ref. [159] with permission, Copyright 2019, Royal Society of Chemistry.

duction over time [105]. On the contrary, NASICON has a large interfacial resistance of 524 Ω cm² which restricts its practical applications [224]. However, heat treatment can improve the surface wettability of sodium metal on solid-state electrolytes. Zhou *et al.* [233] found that after heat treatment of NASICON and sodium at 175 and 380 °C, the interfacial resistance was lowered from 4000 to 400 Ω cm², which was attributed to the improved wettability between NASICON and sodium. Meanwhile, Matios *et al.* [224] grew a regulated graphene-like layer onto NASICON to decrease the interfacial resistance from 524 to 46 Ω cm². This indicates that the layer greatly facilitates Na⁺ conduction across the NASICON/Na interface. Chalcogenide SSEs have small interfacial resistance at the first contact with sodium. But they are very feasible to decomposition to form an MCI, and as a consequence, the interfacial resistance gradually increases with time. For example, Wenzel *et al.* observed that the initial interfacial resistance of Na₃PS₄ with sodium increased from 60 Ω to almost 120 Ω over a period of only 12 h [105]. Similar occurrence was also observed in the case of Na₃SbS₄, where a large increase in the interfacial resistance from 40 Ω cm² to 1000 Ω cm² happened over a period of 50 h [176]. Moreover, it was found that in the case of complex hydrides, they possess a low interfacial resistance of about 50 Ω, which may remain stable over a long period given the better stability of hydrides against sodium metal [201]. However, unfortunately, there is a dearth of data analyzing the interfacial resistance for perovskite and antiperovskite SSEs to compare with other solid-state electrolyte counterparts.

Grain boundary effect is another important factor that affects the solid-state electrolyte's performance. In annealed polycrystalline materials, grain boundaries have a crucial impact on ion transfer. Grain boundary effects are controlled by several parameters, including grain size, grain boundary connectivity, activa-

tion energy and excess free volume [234]. Owing to high mechanical strength and strenuous processing conditions of oxide-based solid-state electrolytes, the effect of grain boundaries on the ion migration is very significant. As a result, the grain boundaries in oxides exhibit larger resistance to migration of ions along the electrolyte and adversely affect the bulk ionic conduction in the material. In addition to high resistivity, the grain boundaries are most vulnerable to the propagation of dendrites in the electrolyte that could derail the performance of the cell [235].

Remedies to address interfacial instability

Solutions to solve the interfacial issues could be divided into two main parts: physical and chemical methods. Physical methods refer majorly to high temperature methods such as hot pressing [236–239]. Hot pressing not only improves the densification of the pellet to enhance ionic conductivity, but also thins down the grain boundaries, reducing its interfacial resistance. However, physical methods are more tedious in nature to be applied on a large scale, which calls for more focus on chemical methods that constitute processes such as composition tuning and artificial SEIs. The following section details solely on the various chemical methods that have been studied so far in improving interfacial properties between the inorganic solid-state electrolyte and the sodium metal anode.

Compositional tuning

Tuning the composition of SSEs by doping or substitution can increase the ionic conductivity of SSEs in addition to addressing certain aspects of the interfacial instability. Halogens are effective dopants for SSEs, especially for chalcogen-based SSEs. Huang and co-workers [240] found that the ionic conductivity of Br-doped

t-Na₃PS₄ is predicted to be 2.37 mS cm⁻¹ via AIMD simulations, while the undoped t-Na₃PS₄ remains to be about 0.01 mS cm⁻¹. Ong and Meng [175] presented a first-principles-guided discovery that Cl-doped Na_{2.9375}PS_{3.9375}Cl_{0.0625} could exhibit a high ionic conductivity of 1.14 mS cm⁻¹ and enhanced electrochemical stability of 0–2.4 V. When it comes to NASICON, as mentioned in the previous section, the Sc doped Na_{3.4}Sc_{0.4}Zr_{1.6}(SiO₄)₂(PO₄) has a wider electrochemical stability window of 0.3–6 V, as compared with 1.75–5 V for pure NASICON [213]. Meanwhile, no obvious chemical reaction with sodium was observed by XPS for Sc doped Na_{3.4}Sc_{0.4}Zr_{1.6}(SiO₄)₂(PO₄), which reflects high chemical stability with sodium of the Sc doped NASICON [166]. This composition of the NASICON electrolyte also exhibited fairly good cyclability up to 100 cycles in a Na_xCoO₂/NASICON/Na full cell and could withstand current densities of the order of 320 μA cm⁻². However, the economic feasibility for large-scale production should be evaluated due to the relatively high cost of scandium. Various metals [211,215,222,241–244], metalloid elements [187,206,220,240,245,246] or clusters [247] have also been employed to improve electrolyte properties and improve their respective stability against sodium metal.

Artificial SEIs

Compositional tuning technique modifies the chemical nature and the crystal structure of the parent material, whereas the arti-

ficial SEI techniques are more extrinsic in nature. A SEI is defined as the layer forming between the liquid electrolyte and the electrode that conducts ions but not electrons. Low electronic conductivity still has non-negligible influence on the dendrite growth within the solid-state electrolytes. Hence, we need to construct an electronic insulation layer to cut off the electron transfer from the electron conductive electrode to the solid-state electrolyte to prevent continuous interface decomposition [101,248,249]. Constructing artificial SEIs is a viable way to withstand electron transfer between the interface of the electrode and the solid-state electrolyte [249,250].

Polymers are proven electron blocking interlayers. Framing a hybrid polymer layer between the electrode and inorganic solid-state electrolyte is an effective mean to block electron transfer. In addition, polymers can also enhance the wettability of SSEs to the sodium metal resulting in a more uniform current distribution and can prevent dendrite growth at high current density regions. The illustrations of the mechanism are shown in Fig. 8a. Zhou et al. [233] introduced *in-situ* formed interfacial interlayer – a dry polymer film formed by cross-linked poly(ethylene glycol) methyl ether acrylate (CPMEA) to improve the wettability of sodium on NASICON. The polymer film gives a uniform Na⁺ flux across the interface, dramatically lowering the interface resistance from 4000 to 1000 Ω (Fig. 8b). The symmetric Na/CPMEA/NASICON/CPMEA/Na cell showed a stable

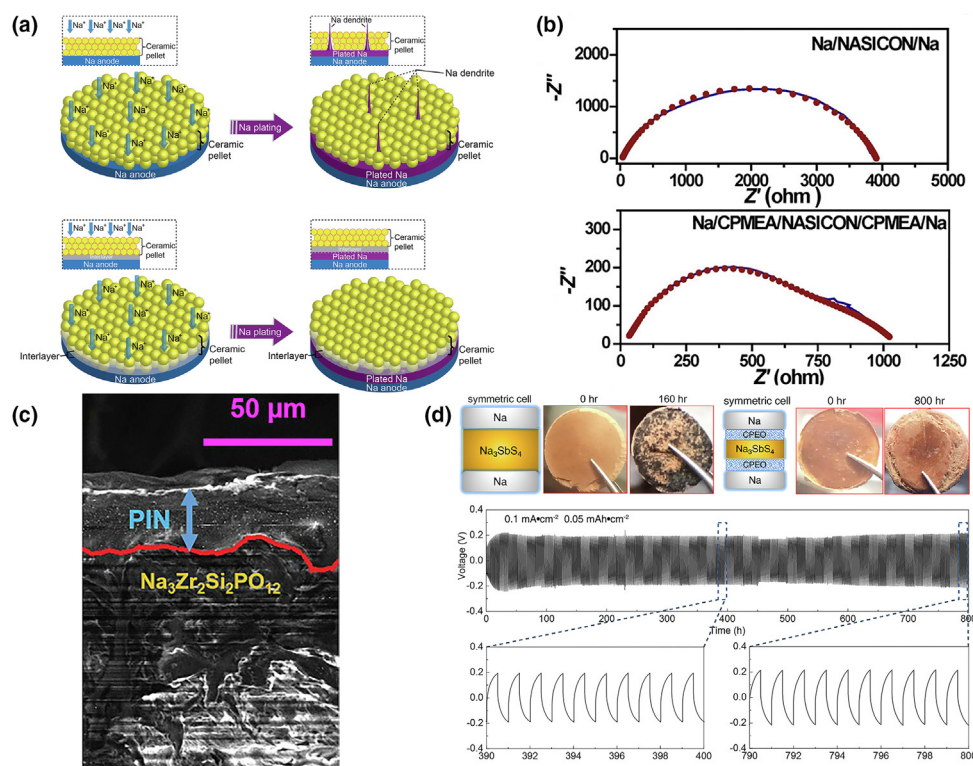


FIGURE 8

(a) A schematic diagram of poor wettability (above) and good wettability (below) of sodium and solid-state electrolyte during Na plating. (b) EIS plots of Na/NASICON/Na and Na/CPMEA/NASICON/CPMEA/Na symmetric cells at 65 °C. Reproduced from Ref. [233] with permission, Copyright 2017, American Chemical Society. (c) SEM image of the cross-section of the PIN-coated Na₃Zr₂Si₂PO₁₂ membrane. Reproduced from Ref. [251] with permission, Copyright 2019, Elsevier. (d) CPEO coated (right) and uncoated (left) Na₃SbS₄ contact with sodium after several hours (above), the sodium plating and stripping performance of Na/CPEO/Na₃SbS₄/CPEO/Na symmetric cells (below) at the current density of 0.1 mA cm⁻². Reproduced from Ref. [252] with permission, Copyright 2019, American Chemical Society.

voltage profile for up to 380 h under a continuous current density of 0.20 mA cm^{-2} at 65°C . This indicates that undesirable sodium dendrites are successfully suppressed, in addition to exhibiting a high coulombic efficiency over several cycles.

Furthermore, the same solution was also used for the case of lithium aluminum titanium phosphate (LATP) [253]. Yu et al. [251] put forward the idea of coating a layer of a polymer with intrinsic nanoporosity (PIN) membrane onto $\text{Na}_3\text{Zr}_2\text{Si}_2\text{PO}_{12}$. The SEM image, shown in Fig. 8c, shows a tight contact between PIN and NASICON. The PIN layer greatly improves the ionic interfacial properties between sodium and $\text{Na}_3\text{Zr}_2\text{Si}_2\text{PO}_{12}$. This is clear since the sodium-sulfur $\text{Na}||\text{Na}_3\text{Zr}_2\text{Si}_2\text{PO}_{12}||\text{CNF/S}$ cell exhibits a much higher impedance than the $\text{Na}||\text{PIN-Na}_3\text{Zr}_2\text{Si}_2\text{PO}_{12}||\text{CNF/S}$ cell, before and after cycling. The latter even exhibited better cycle performance than liquid electrolyte batteries due to the inhibition of polysulfide migration from the cathode. Hu et al. [252] proposed a cellulose-poly(ethylene oxide) (CPEO) interlayer to stabilize the interface between sulfide electrolyte Na_3SbS_4 and sodium, as shown in Fig. 8d. The pristine Na_3SbS_4 pellet was reduced by sodium with macroscopic changes on the surface after 160 h. However, the CPEO-protected pellet exhibited excellent stability against sodium until 800 h. The all-solid-state devices could achieve stable Na stripping/plating for 800 cycles at 0.1 mA cm^{-2} at 60°C . In the case of β' -alumina, interestingly, the removal of surface hydroxy groups and carbon contamination by subjecting the ceramics to heat treatment at 1600°C in the presence of argon atmosphere helped drastically reduce the internal resistance to $8 \Omega \text{ cm}^{-2}$ from several hundred $\Omega \text{ cm}^{-2}$. This facile technique has also led to an increase in the critical current density of the order of 12 mA cm^{-2} for a total transferred charge density of 0.25 mAh cm^{-2} per half cycle from 0.3 mA cm^{-2} [254].

Since limited research has been done on artificial SEIs for sodium-based solid-state electrolyte systems, one could take some inspiration from SEIs fabricated for lithium-based counterparts. Wang et al. [255] presented a plastic crystal electrolyte-succinonitrile (SN)-based electrolyte with good thermal stability and non-flammability. It shows great promise as a safe electrolyte and demonstrated that the significant interfacial reactions between sulfide-based SSEs and Li metal could be suppressed. Zhou et al. [256] fabricated PEO-poly aluminum sulfate (PAS) electrolyte membrane as the polymer-ceramic single-ion-conducting solid-state electrolyte (PCSSE) coating on the ceramic LLZTO pellet. This demonstrated good adhesion to the ceramic electrolyte and lithium metal for a homogenous interface. It also isolated direct contact between the lithium-metal anode and the grain boundaries of LLZTO pellet. Chi et al. [257] came up with introducing a solid polymer electrolyte (SPE) soft interface layer deposited on garnet LLZTO electrolyte. The SPE could endow connected interface between the electrolyte and electrodes settling the interface contact issue. SPE serving as the electron insulator is a kind of user-friendly sandwich material to ameliorate the interface instability.

Sodium alloying

Sodium alloying is another way to improve the intrinsic safety, reduce dendrite formation and passivate the surface layer. This not only provides the high capacity but also avoids the low elec-

trochemical potential of sodium metal, especially for chalcogenide electrolytes [258,259]. A US patent presented a sodium battery which reports on a cell constituting a solid-state electrolyte and an engineered metallization layer that distributes sodium across the surface of the electrolyte could enhance the performance, efficiency, and capacity at intermediate temperatures (below or about 200°C). This metallization layer of materials (with a thickness below five microns) include Pt, Au, Ag, Ni, Cu, Sn, Pb and their alloys [260]. It is known that the wettability of sodium $\beta''\text{-Al}_2\text{O}_3$ and sodium is not that good, sodium $\beta''\text{-Al}_2\text{O}_3$ single cells need to operate at high temperature of $300\text{--}350^\circ\text{C}$. Lu et al. [261] reported a Na-Cs alloying strategy to markedly improve the wettability of sodium $\beta''\text{-Al}_2\text{O}_3$ at low temperatures. The Na-S single cell with Na-Cs as the anode presented huge improvement in cycle life at 150 and 175°C over pristine sodium as the anode. Furthermore, even at temperatures as low as 95°C , the cell still exhibited good electrochemical performances with a high capacity of 330 mAh g^{-1} . This in turn could avoid the intrinsic safety issues associated with high temperatures for battery operation. Hayashi et al. [173] applied Na-Sn alloy as the anode to fabricate Na-Sn/ Na_3PS_4 glass-ceramic/ TiS_2 cells, which showed a reversible capacity of about 90 mAh g^{-1} for 10 cycles with no obvious capacity fade. Chevrier and co-workers [82] investigated the Na-Sn alloy and observed that the electrochemical sodiation of Sn could uptake 3.75 Na's per Sn, suggesting that $\text{Na}_{1.5}\text{Sn}_4$ alloy is a potential anode for sodium batteries.

There are still other solutions to improve interfacial properties. For sodium β -alumina, the best way to optimize the interfacial issue is to melt the sodium metal and operate the battery at high temperatures [262]. For the solid-state electrolyte itself, Fitzhugh et al. and Wu et al. [116,232] proposed a structure design of SSEs with core-shell structures that is another advanced strategy for the next generation sulfide-based all-solid-state batteries. By controlling synthesis parameters, the consequent core-shell microstructure for Li-Si-P-S and Li-Ge-P-S sulfide electrolytes results in a stability window from 0.7 to $3.1\text{--}4.0 \text{ V}$, with an amorphous shell of high Si composition to provide the materials-level mechanical constriction, which is much larger than the previously predicted one of $1.7\text{--}2.1 \text{ V}$. These days, computational methods have gained more attention and a high-throughput search for materials with specific demands in the database saves both time and labor. Fitzhugh et al. [263] put forward a high-throughput search for functionally stable interface coating materials for $\text{Li}_{10}\text{SiP}_2\text{S}_{12}$ (LSPS) in a widened voltage window by assuming that proper mechanical constrictions to the bulk had been applied [232], where valuable coating materials for both cathode and anode sides were predicted. Such high-throughput search methods will also speed up the design of the next generation sodium based solid-state batteries with superior interfacial properties.

Closing remarks

To conclude, we have highlighted different types of interfaces that form during the electrochemical interaction between sodium-based inorganic solid-state electrolytes and sodium metal, and further addressed the key issues that affect the perfor-

mance of an all-solid-state sodium metal battery. The chemical stability of the interface, the mechanical stability of the electrolyte, the ionic and electronic conductivities of the electrolyte, and the interfacial resistance based on the wettability of the electrolytes are some of the most important aspects covered in this review.

By categorizing the electrolytes based on their compositions, major causes for interfacial and electrolyte instabilities have been accounted for. The chemical instabilities against sodium metal and the low mechanical strength have hampered the progress in the application of highly conductive chalcogenide materials. The generally poor air-stability to generate hazardous substances, such as hydrogen sulfide, also needs to be addressed for practical applications. Complex hydrides, on the other hand, were found to be highly stable against sodium metal but their mechanical strength needs improvement to be used efficiently in an all-solid-state battery. The lack of detailed studies on perovskites and anti-perovskites leaves the door wide open for researchers to explore. At present, it remains that sodium β -alumina could be the most amicable option as a solid-state electrolyte for its excellent ionic conductivity, chemical stability against sodium metal, good mechanical properties and negligible electronic conductivity. However, much effort needs to be made to ameliorate the strenuous processing conditions that negate its practical efficiency without compromising other properties. Furthermore, Na metal is even softer than Li, with a number of electrolyte materials showing absolute thermodynamic stability against Na metal (such as phosphates, borates and silicates), making them more likely to achieve chemical/mechanical stability at the Na/electrolyte interface compared with the lithium counterparts.

The future of all-solid-state sodium metal-based batteries falls on mainly three facets of research and development. The first is to discover new materials exhibiting high ionic conductivity and still satisfying other various properties mentioned before. Although far-fetched, there are still various avenues, *e.g.*, with the support of high-throughput computational techniques, one could venture to identify new structures and chemistries that possess superior properties. The second is to further understand and unravel the fundamental mechanisms of interfacial reactions and ionic conduction across the interface with specifically designed *in-situ* experiments and sophisticated instruments. Understanding the physical and chemical aspects of the sodium metal–solid electrolyte interface would also allow researchers to recognize the underlying chemo-mechanical effects and critical current densities that could otherwise hamper cyclability of all-solid-state sodium metal-based batteries. The insights obtained from these studies will also be very helpful when addressing the third facet, which is to find alternative ways to address specific issues with the electrolytes and eradicate their undesirable properties without adversely affecting their inherent properties. To do that, interface engineering and suitable coating materials are the two mainstream directions that one could investigate.

Declaration of Competing Interest

The authors declare that they have no known competing financial interests or personal relationships that could have appeared to influence the work reported in this paper.

Acknowledgements

This work was supported by NSFC (21773126) and Shanghai Sailing Program (Contract No. 18YF1411100). One of the authors P. W. Jaschin acknowledges China Postdoctoral Council for the fellowship provided under the Postdoctoral International Exchange Scheme. The authors would also like to thank Sri Uma Aisvarya and Houhe Liu for proofreading the manuscript.

References

- [1] Whittingham, M. S., Proc. IEEE (2012) 100 (Special Centennial Issue), 1518.
- [2] Z.Z. Zhang et al., Energy Environ. Sci. 11 (8) (2018) 1945.
- [3] N. Kamaya et al., Nat. Mater. 10 (9) (2011) 682.
- [4] P. Canepa et al., Nat. Commun. 8 (1) (2017) 1759.
- [5] A. Manthiram et al., Nat. Rev. Mater. 2 (4) (2017) 16103.
- [6] G.T. Hitz et al., Mater. Today 22 (2019) 50.
- [7] J. Lu et al., Nat. Nanotechnol. 11 (12) (2016) 1031.
- [8] Y. Gao et al., Chem. Rev. 120 (13) (2020) 5954.
- [9] E. Quartarone, P. Mustarelli, Chem. Soc. Rev. 40 (5) (2011) 2525.
- [10] J.C. Bachman et al., Chem. Rev. 116 (1) (2016) 140.
- [11] H. Zhang et al., Chem. Soc. Rev. 46 (3) (2017) 797.
- [12] K. Kang et al., Science 311 (5763) (2006) 977.
- [13] Y. Essamlali et al., Renew. Energy 133 (2019) 1295.
- [14] N. Yabuuchi et al., Chem. Rev. 114 (23) (2014) 11636.
- [15] J. Peters et al., Energy Environ. Sci. 9 (5) (2016) 1744.
- [16] K. Kubota, S. Komaba, J. Electrochem. Soc. 162 (14) (2015) A2538.
- [17] X. Xiang et al., Adv. Mater. 27 (36) (2015) 5343.
- [18] L.L. Wong et al., Phys. Chem. Chem. Phys. 19 (11) (2017) 7506.
- [19] I. Hasa et al., ACS Appl. Mater. Interfaces 7 (9) (2015) 5206.
- [20] I. Hasa et al., Adv. Energy Mater. 4 (15) (2014) 1400083.
- [21] L. Mu et al., Adv. Mater. 27 (43) (2015) 6928.
- [22] S. Kumakura et al., Angew. Chem. Int. Ed. 55 (41) (2016) 12760.
- [23] A. Moretti et al., ChemElectroChem 2 (4) (2015) 529.
- [24] D. Carlier et al., Dalton Trans. 40 (36) (2011) 9306.
- [25] H. Wang et al., Electrochim. Acta 113 (2013) 200.
- [26] S. Komaba et al., Inorg. Chem. 51 (11) (2012) 6211.
- [27] X. Rong et al., J. Electrochem. Chem. 31 (2019) 132.
- [28] Y.-E. Zhu et al., J. Mater. Chem. A 4 (28) (2016) 11103.
- [29] C. Ma et al., J. Am. Chem. Soc. 139 (13) (2017) 4835.
- [30] B.M. De Boisse et al., J. Electrochem. Soc. 160 (4) (2013) A569.
- [31] H. Wang et al., J. Electrochem. Soc. 163 (3) (2016) A565.
- [32] Y. Liu et al., Nano Lett. 16 (5) (2016) 3321.
- [33] M. Guignard et al., Nat. Mater. 12 (1) (2013) 74.
- [34] Y.S. Meng et al., Phys. Rev. B 72 (17) (2005) 172103.
- [35] Y. Zhang et al., J. Electrochem. Soc. 165 (7) (2018) A1184.
- [36] Y. Wang et al., Nat. Commun. 4 (2013) 2365.
- [37] K. Zhang et al., Adv. Funct. Mater. 26 (37) (2016) 6728.
- [38] B. Qu et al., Adv. Mater. 26 (23) (2014) 3854.
- [39] Z. Hu et al., Energy Environ. Sci. 8 (4) (2015) 1309.
- [40] Z. Hu et al., Angew. Chem. Int. Ed. 53 (47) (2014) 12794.
- [41] Z. Jian et al., Electrochem. Commun. 14 (1) (2012) 86.
- [42] K.T. Lee et al., Chem. Mater. 23 (16) (2011) 3593.
- [43] H. Li et al., Chem. Mater. 30 (8) (2018) 2498.
- [44] K. Trad et al., Chem. Mater. 22 (19) (2010) 5554.
- [45] W. Duan et al., J. Mater. Chem. A 2 (23) (2014) 8668.
- [46] B. Ellis et al., Nat. Mater. 6 (10) (2007) 749.
- [47] L. Sharma et al., ACS Appl. Mater. Interfaces 9 (40) (2017) 34961.
- [48] R. Gond et al., Inorg. Chem. 57 (11) (2018) 6324.
- [49] G.S. Shinde et al., Mater. Res. Express 7 (1) (2019) 014001.
- [50] W. Luo et al., Accounts. Chem. Res. 49 (2) (2016) 231.
- [51] J. Xu et al., Funct. Mater. Lett. 6 (01) (2013) 1330001.
- [52] F. Xie et al., Adv. Funct. Mater. 29 (24) (2019) 1970164.
- [53] L. Fu et al., Nanoscale 6 (3) (2014) 1384.
- [54] C. Zhu et al., Angew. Chem. Int. Ed. 53 (8) (2014) 2152.
- [55] S. Komaba et al., Adv. Funct. Mater. 21 (20) (2011) 3859.
- [56] R. Raccichini et al., Nat. Mater. 14 (3) (2015) 271.
- [57] Z. Jian et al., Adv. Energy Mater. 6 (3) (2016) 1501874.
- [58] Y. Li et al., Adv. Energy Mater. 6 (18) (2016) 1600659.
- [59] X. Dou et al., Mater. Today 23 (2019) 87.
- [60] S. Peng et al., Small 12 (10) (2016) 1359.
- [61] Y. Liu et al., Adv. Funct. Mater. 25 (2) (2015) 214.

- [62] B. Farbod et al., *ACS Nano* 8 (5) (2014) 4415.
- [63] M.-S. Balogun et al., *Carbon* 98 (2016) 162.
- [64] M. Lao et al., *Adv. Mater.* 29 (48) (2017) 1700622.
- [65] Y. Zhao, A. Manthiram, *Chem. Mater.* 27 (8) (2015) 3096.
- [66] H. Che et al., *Energy Environ. Sci.* 10 (5) (2017) 1075.
- [67] Y. Shao et al., *Energy Storage Mater.* 23 (2019) 514.
- [68] A. Hayashi et al., *Nat. Commun.* 10 (1) (2019) 5266.
- [69] A. Bauer et al., *Adv. Energy Mater.* 8 (17) (2018) 1702869.
- [70] Department, S. a. T., The first low-speed electric vehicle with sodium ion batteries was unveiled in China, http://www.iop.cas.cn/xwzx/snxw/201806/t20180608_5024146.html, 2018..
- [71] C. Zhao et al., *Adv. Energy Mater.* 8 (17) (2018) 1703012.
- [72] D. Lei et al., *Nat. Commun.* 10 (1) (2019) 4244.
- [73] M.M. Doeff et al., *Electrochim. Acta* 40 (1995) 2205.
- [74] R.P. Rao et al., *J. Mater. Chem. A* 5 (7) (2017) 3377.
- [75] D. Stevens, J. Dahn, *J. Electrochem. Soc.* 147 (4) (2000) 1271.
- [76] L. Ye et al., *Angew. Chem. Int. Edit.* 58 (47) (2019) 17054.
- [77] L. Fan, X. Li, *Nano Energy* 53 (2018) 630.
- [78] T. Famprikis et al., *Nat. Mater.* 18 (12) (2019) 1278.
- [79] L. Froboese et al., *J. Electrochem. Soc.* 166 (2) (2019) A318.
- [80] J. Janek, W.G. Zeier, *Nat. Energy* 1 (9) (2016) 16141.
- [81] H. Li et al., *Solid State Ionics* 318 (2018) 1.
- [82] V.L. Chevrier, G. Ceder, *J. Electrochem. Soc.* 158 (9) (2011) A1011.
- [83] R. Nölle et al., *Mater. Today* 32 (2020) 131.
- [84] R. Koerver et al., *J. Mater. Chem. A* 5 (43) (2017) 22750.
- [85] A.M. Nolan et al., *ACS Energy Lett.* 4 (10) (2019) 2444.
- [86] K. Nie et al., *Front. Chem.* 6 (2018) 616.
- [87] J.Q. Dai et al., *Adv. Mater.* 30 (48) (2018) e1802068.
- [88] J.P. Yue et al., *Adv. Funct. Mater.* 28 (38) (2018) 1707533.
- [89] Z. Ahmad, V. Viswanathan, *Phys. Rev. Lett.* 119 (5) (2017) 056003.
- [90] J. Nissen et al., *Phys. Rev. Lett.* 86 (9) (2001) 1904.
- [91] X. Zheng et al., *Phys. Rev. Lett.* 74 (3) (1995) 407.
- [92] Y.Z. Zhu et al., *ACS Appl. Mater. Interfaces* 7 (42) (2015) 23685.
- [93] R. Koerver et al., *Energy Environ. Sci.* 11 (8) (2018) 2142.
- [94] Y.Z. Zhu et al., *J. Mater. Chem. A* 4 (9) (2016) 3253.
- [95] A.M. Nolan et al., *Joule* 2 (10) (2018) 2016.
- [96] C.-Z. Zhao et al., *Energy Storage Mater.* 24 (2020) 75.
- [97] Y. Xiao et al., *Nat. Rev. Mater.* 5 (2) (2019) 105.
- [98] Y. Yui et al., *Sci. Rep.* 6 (2016) 22406.
- [99] R. Rodriguez et al., *ACS Energy Lett.* 2 (9) (2017) 2051.
- [100] S. Wei et al., *Adv. Mater.* 29 (2017) 12.
- [101] B. Lee et al., *Chem. Rev.* 119 (8) (2019) 5416.
- [102] Y. Lu et al., *Joule* 2 (9) (2018) 1747.
- [103] C. Zhao et al., *Angew. Chem. Int. Ed.* 58 (47) (2019) 17026.
- [104] T. Krauskopf et al., *ACS Appl. Mater. Interfaces* 11 (15) (2019) 14463.
- [105] S. Wenzel et al., *ACS Appl. Mater. Interfaces* 8 (41) (2016) 28216.
- [106] G.F. Dewald et al., *Chem. Mater.* 31 (20) (2019) 8328.
- [107] S. Wenzel et al., *Chem. Mater.* 28 (7) (2016) 2400.
- [108] T. Krauskopf et al., *Joule* 3 (8) (2019) 2030.
- [109] E.J. Cheng et al., *Electrochim. Acta* 223 (2017) 85.
- [110] L. Miara et al., *ACS Appl. Mater. Interfaces* 8 (40) (2016) 26842.
- [111] W.D. Richards et al., *Chem. Mater.* 28 (1) (2015) 266.
- [112] X.D. Zhao et al., *J. Mater. Chem. A* 6 (6) (2018) 2625.
- [113] G. Ceder et al., *Mrs. Bull.* 43 (10) (2018) 746.
- [114] A. Jain et al., *APL Mater.* 1 (1) (2013) 011002.
- [115] W. Fitzhugh et al., *J. Mater. Chem. A* 7 (41) (2019) 23604.
- [116] W. Fitzhugh et al., *Small* 15 (33) (2019) 1901470.
- [117] Z. Wang et al., *Nano Lett.* 16 (6) (2016) 3760.
- [118] Y.S. Tian et al., *Joule* 3 (4) (2019) 1037.
- [119] H.C. Gao et al., *Chem* 4 (4) (2018) 833.
- [120] S. Appelt et al., *Nat. Phys.* 2 (2) (2006) 105.
- [121] L. Xu et al., *Joule* 2 (10) (2018) 1991.
- [122] C. Monroe, J. Newman, *J. Electrochem. Soc.* 152 (2) (2005) A396.
- [123] P. Albertus et al., *Nat. Energy* 3 (1) (2017) 16.
- [124] A. Mauger et al., *J. Power Sources* 353 (2017) 333.
- [125] C. Xu et al., *Proc. Natl. Acad. Sci. U.S.A.* 114 (1) (2017) 57.
- [126] S. Yu et al., *Chem. Mater.* 28 (1) (2015) 197.
- [127] T. Watanabe et al., *J. Power Sources* 423 (2019) 255.
- [128] J.A. Lewis et al., *ACS Energy Lett.* 4 (2) (2019) 591.
- [129] F. Aguesse et al., *ACS Appl. Mater. Interfaces* 9 (4) (2017) 3808.
- [130] K.J. Griffith et al., *J. Am. Chem. Soc.* 141 (42) (2019) 16706.
- [131] P. Hartmann et al., *J. Phys. Chem. C* 117 (41) (2013) 21064.
- [132] F.P. McGrogan et al., *Adv. Energy Mater.* 7 (12) (2017) 1602011.
- [133] K.N. Wood et al., *ACS Energy Lett.* 2 (3) (2017) 664.
- [134] P. Wang et al., *Adv. Funct. Mater.* 29 (27) (2019) 1900950.
- [135] G. Bucci et al., *J. Mater. Chem. A* 5 (36) (2017) 19422.
- [136] N. Sun et al., *Angew. Chem. Int. Edit.* 58 (51) (2019) 18647.
- [137] G. Bucci et al., *Phys. Rev. Mater.* 2 (10) (2018) 105407.
- [138] R. Garcia-Mendez et al., *Electrochim. Acta* 237 (2017) 144.
- [139] J. Wolfenstine et al., *Ionics* 24 (5) (2017) 1271.
- [140] P. Li et al., *J. Phys. Energy* 2 (2020) 2.
- [141] J.A. Lewis et al., *Trends Chem.* 1 (9) (2019) 845.
- [142] J. Tippens et al., *ACS Energy Lett.* 4 (6) (2019) 1475.
- [143] P. Wang et al., *Adv. Funct. Mater.* (2019).
- [144] R. Chen et al., *Chem. Rev.* 120 (14) (2020) 6820.
- [145] J. Kasemchainan et al., *Nat. Mater.* 18 (10) (2019) 1105.
- [146] J.M. Doux et al., *Adv. Energy Mater.* 10 (2019) 1.
- [147] Y. Su et al., *Energy Environ. Sci.* 13 (3) (2020) 908.
- [148] Z. Ding et al., *J. Electrochem. Soc.* 167 (2020) 7.
- [149] D. Spencer Jolly et al., *ACS Appl. Mater. Interfaces* 12 (1) (2020) 678.
- [150] M.V.F. Heinz et al., *J. Power Sources* 465 (2020) 228268.
- [151] Y.J. Nam et al., *J. Mater. Chem. A* 6 (30) (2018) 14867.
- [152] L. Porz et al., *Adv. Energy Mater.* 7 (2017) 20.
- [153] Y.-F.-Y. Yao, J. Kummer, *J. Inorg. Nucl. Chem.* 29 (9) (1967) 2453.
- [154] M.S. Whittingham, R.A. Huggins, *J. Chem. Phys.* 54 (1) (1971) 414.
- [155] K. Kim et al., *J. Phys. Chem. Solids* 40 (10) (1979) 743.
- [156] S.-T. Lee et al., *B. Mater. Sci.* 39 (3) (2016) 729.
- [157] X.C. Lu et al., *J. Power Sources* 195 (9) (2010) 2431.
- [158] S.-I. Kim et al., *J. Korean Cryst. Growth Cryst. Technol.* 24 (4) (2014) 164.
- [159] V. Lacivita et al., *J. Mater. Chem. A* 7 (14) (2019) 8144.
- [160] J.B. Goodenough et al., *Mater. Res. Bull.* 11 (2) (1976) 203.
- [161] H.-P. Hong, *Mater. Res. Bull.* 11 (2) (1976) 173.
- [162] J.P. Boilot et al., *Mater. Res. Bull.* 22 (5) (1987) 669.
- [163] Z. Zhang et al., *Adv. Energy Mater.* 9 (42) (2019) 1902373.
- [164] M. Guin, F. Tietz, *J. Power Sources* 273 (2015) 1056.
- [165] N. Anantharamulu et al., *J. Mater. Sci.* 46 (9) (2011) 2821.
- [166] P. Kehne et al., *J. Power Sources* 409 (2019) 86.
- [167] Z. Zhang et al., *Adv. Energy Mater.* 7 (4) (2017) 1601196.
- [168] X. Han et al., *Nat. Mater.* 16 (5) (2017) 572.
- [169] W. Luo et al., *J. Am. Chem. Soc.* 138 (37) (2016) 12258.
- [170] C.P. Yang et al., *Adv. Mater.* 31 (3) (2019) e1804815.
- [171] K.H. Park et al., *Adv. Energy Mater.* 8 (18) (2018) 1800035.
- [172] M. Jansen, U. Henseler, *J. Solid State Chem.* 99 (1992) 110.
- [173] A. Hayashi et al., *Nat. Commun.* 3 (2012) 856.
- [174] A. Hayashi et al., *J. Power Sources* 258 (2014) 420.
- [175] I.H. Chu et al., *Sci. Rep.* 6 (2016) 33733.
- [176] E.A. Wu et al., *ACS Appl. Mater. Interfaces* 10 (12) (2018) 10076.
- [177] J. Heyd et al., *J. Chem. Phys.* 118 (18) (2003) 8207.
- [178] K.N. Wood et al., *Nat. Commun.* 9 (1) (2018) 2490.
- [179] S.H. Bo et al., *J. Mater. Chem. A* 4 (23) (2016) 9044.
- [180] L. Zhang et al., *Adv. Energy Mater.* 5 (24) (2015) 1501294.
- [181] Y.S. Tian et al., *Energy Environ. Sci.* 10 (5) (2017) 1150.
- [182] A. Abouimrane et al., *J. Am. Chem. Soc.* 134 (10) (2012) 4505.
- [183] H. Wang et al., *Angew. Chem. Int. Edit.* 55 (30) (2016) 8551.
- [184] L. Zhang et al., *Adv. Sci.* 3 (10) (2016) 1600089.
- [185] T.W. Kim et al., *J. Mater. Chem. A* 6 (3) (2018) 840.
- [186] A. Banerjee et al., *Angew. Chem. Int. Edit.* 55 (33) (2016) 9634.
- [187] K.H. Park et al., *J. Mater. Chem. A* 6 (35) (2018) 17192.
- [188] W.D. Richards et al., *Nat. Commun.* 7 (2016) 11009.
- [189] J.W. Heo et al., *Adv. Energy Mater.* 8 (2018) 11.
- [190] E.P. Ramos et al., *Chem. Mater.* 30 (21) (2018) 7413.
- [191] M. Duchardt et al., *Chem. Mater.* 30 (12) (2018) 4134.
- [192] Z. Zhang et al., *Energy Environ. Sci.* 11 (1) (2018) 87.
- [193] Z.X. Yu et al., *Nano Energy* 47 (2018) 325.
- [194] Z.X. Yu et al., *Energy Storage Mater.* 17 (2019) 70.
- [195] L. Duchene et al., *Chem. Commun.* 53 (30) (2017) 4195.
- [196] H. Oguchi et al., *J. Appl. Phys.* 111 (3) (2012) 036102.
- [197] M.J. van Setten et al., *Phys. Rev. B* 75 (3) (2007) 035204.
- [198] T.J. Udovic et al., *Adv. Mater.* 26 (45) (2014) 7622.
- [199] H.C. Chen, T. Hong, *J. Electrochem. Soc.* 166 (4) (2019) A493.
- [200] K. Yoshida et al., *Appl. Phys. Lett.* 110 (10) (2017) 103901.
- [201] L. Duchêne et al., *Energy Environ. Sci.* 10 (12) (2017) 2609.
- [202] D.N. Rajendran et al., *Mater. Chem. Phys.* 109 (2–3) (2008) 189.
- [203] Y.Z. Zhao et al., *J. Alloy. Compd.* 783 (2019) 219.
- [204] X. Lu et al., *Chem. Commun.* 50 (78) (2014) 11520.
- [205] J. Ramanna et al., *Solid State Sci.* 20 (2013) 120.

- [206] Y.G. Wang et al., *J. Appl. Phys.* 119 (2) (2016) 025901.
- [207] S.J. Choi et al., *ACS Appl. Mater. Interfaces* 10 (37) (2018) 31404.
- [208] J. Briant, G. Farrington, *J. Solid State Chem.* 33 (3) (1980) 385.
- [209] Y.L. Ruan et al., *Ceram. Int.* 45 (2) (2019) 1770.
- [210] S. Narayanan et al., *Solid State Ionics* 331 (2019) 22.
- [211] D. Chen et al., *J. Alloy. Compd.* 757 (2018) 348.
- [212] Y. Ruan et al., *Ceram. Int.* 43 (10) (2017) 7810.
- [213] Q.L. Ma et al., *Chem. Mater.* 28 (13) (2016) 4821.
- [214] C.K. Moon et al., *ACS Energy Lett.* 3 (10) (2018) 2504.
- [215] N. Wang et al., *J. Mater. Sci.* 53 (3) (2017) 1987.
- [216] N. Tanibata et al., *RSC Advances* 4 (33) (2014) 17120.
- [217] Y. Sun et al., *J. Am. Chem. Soc.* 141 (14) (2019) 5640.
- [218] H. Nguyen et al., *J. Electrochem. Soc.* 163 (10) (2016) A2165.
- [219] J. Zhu et al., *Inorg. Chem.* 55 (12) (2016) 5993.
- [220] Y.G. Wang et al., *J. Power Sources* 293 (2015) 735.
- [221] F.D. Han et al., *Nat. Energy* 4 (3) (2019) 187.
- [222] A.G. Jolley et al., *Ionics* 21 (11) (2015) 3031.
- [223] T.H. Wan et al., *J. Power Sources* 390 (2018) 61.
- [224] E. Matios et al., *ACS Appl. Mater. Interfaces* 11 (5) (2019) 5064.
- [225] D.C. Hitchcock, L.C. De Jonghe, *J. Am. Ceram. Soc.* 66 (11) (1983) c204.
- [226] M. Chen et al., *Science* 300 (5623) (2003) 1275.
- [227] Z. Deng et al., *J. Electrochem. Soc.* 163 (2) (2015) A67.
- [228] A. Sakuda et al., *Sci. Rep.* 3 (2013) 2261.
- [229] M. Nose et al., *J. Mater. Chem. A* 3 (44) (2015) 22061.
- [230] H. Tang et al., *Chem. Mater.* 30 (1) (2017) 163.
- [231] S. Takeuchi et al., *J. Solid State Chem.* 265 (2018) 353.
- [232] F. Wu et al., *Nat. Commun.* 9 (1) (2018) 4037.
- [233] W.D. Zhou et al., *ACS Central Sci.* 3 (1) (2017) 52.
- [234] A. Oudriss et al., *Acta Mater.* 60 (19) (2012) 6814.
- [235] Y.S. Jung et al., *Israel J. Chem.* 55 (5) (2015) 472.
- [236] Y. Noguchi et al., *Electrochim. Acta* 101 (2013) 59.
- [237] A. Aboulaich et al., *Adv. Energy Mater.* 1 (2) (2011) 179.
- [238] Y. Seino et al., *Energy Environ. Sci.* 7 (2) (2014) 627.
- [239] R. Kali, A. Mukhopadhyay, *J. Power Sources* 247 (2014) 920.
- [240] H. Huang et al., *Phys. Chem. Chem. Phys.* 20 (31) (2018) 20525.
- [241] Y. Lu et al., *Adv. Energy Mater.* 9 (28) (2019) 1901205.
- [242] Y. Deng et al., *Chem. Mater.* 30 (8) (2018) 2618.
- [243] Z.Y. Zhu et al., *Chem. Mater.* 27 (24) (2015) 8318.
- [244] A.G. Jolley et al., *J. Am. Ceram. Soc.* 98 (9) (2015) 2902.
- [245] X. Feng et al., *Adv. Funct. Mater.* 29 (9) (2019) 1807951.
- [246] N.J.J. de Klerk, M. Wagemaker, *Chem. Mater.* 28 (9) (2016) 3122.
- [247] H. Fang, P. Jena, *ACS Appl. Mater. Interfaces* 11 (1) (2018) 963.
- [248] Pesci, M. Federico, et al., *J. Mater. Chem. A* 6 (40) (2018) 19817.
- [249] F. Mo et al., *Adv. Energy Mater.* 9 (40) (2019) 1902123.
- [250] E. Matios et al., *Ind. Eng. Chem. Res.* 58 (23) (2019) 9758.
- [251] X. Yu, A. Manthiram, *Matter* 1 (2) (2019) 439.
- [252] P. Hu et al., *ACS Appl. Mater. Interfaces* 11 (10) (2019) 9672.
- [253] W. Zhou et al., *J. Am. Chem. Soc.* 138 (30) (2016) 9385.
- [254] M.C. Bay et al., *Adv. Energy Mater.* 10 (3) (2020) 1902899.
- [255] C. Wang et al., *Adv. Funct. Mater.* 29 (26) (2019) 1900392.
- [256] W.D. Zhou et al., *Nano Energy* 53 (2018) 926.
- [257] S.S. Chi et al., *Energy Storage Mater.* 17 (2019) 309.
- [258] B.L. Ellis, L.F. Nazar, *Curr. Opin. Solid State Mater. Sci.* 16 (4) (2012) 168.
- [259] J. Lau et al., *Adv. Energy Mater.* 8 (27) (2018) 1800933.
- [260] J.Y. Kim et al., *Metallization pattern on solid electrolyte or porous support of sodium battery process*, Google Patents US (2016).
- [261] X. Lu et al., *Nat. Commun.* 5 (1) (2014) 4578.
- [262] T.C. Girija, A.V. Virkar, *J. Power Sources* 180 (1) (2008) 653.
- [263] W. Fitzhugh et al., *Adv. Energy Mater.* 9 (21) (2019) 1900807.